Quality Evaluation for Measurements of Wind Field and Turbulent Flux from a UAV-based Eddy Covariance System

Yibo Sun[1,2,3], Bilige Sude[1,2,3], Xingwen Lin[4], Bing Geng[5], Bo Liu[1,2,3], Shengnan Ji[1,2,3], Junping Jing[6], Zhiping Zhu[7,8], Ziwei Xu[9], Shaomin Liu[9], and Zhanjun Quan[1,2,3]

[1]State Key Laboratory of Environmental Criteria and Risk Assessment, Chinese Research Academy of Environmental Sciences, Beijing 100012, China.
[2]Institute of Ecology, Chinese Research Academy of Environmental Sciences, Beijing 100012, China.
[3]State Environmental Protection Key Laboratory of Ecological Regional Processes and Functions Assessment, Beijing 100012, China.
[4]Collage of Geography and Environment Science, Zhejiang Normal University, Zhejiang 321004, China.
[5]Beijing Academy of Social Sciences, Beijing 100101, China.
[6]National Ocean Technology Center, Tianjin 300112, China.
[7]Kunming General Survey of Natural Resources Center, China Geological Survey, Kunming 650111, China.
[8]Technology Innovation Center for Natural Ecosystem Carbon Sink, Ministry of Natural Resources, Kunming 650100, China.
[9]State Key Laboratory of Earth Surface Processes and Resource Ecology, Faculty of Geographical Science, Beijing Normal University, Beijing 100875, China.

Correspondence to: Bilige Sude (sude@craes.org.cn) and Shaoming Liu (smliu@bnu.edu.cn)

Abstract. Instrumentation packages for eddy covariance (EC) measurements have been developed for unmanned aerial vehicle (UAV) to measure the turbulent fluxes of latent heat (LE), sensible heat (H), and CO_2 (Fc) in the atmospheric boundary layer. This study aims to evaluate the performance of this UAV-based EC system. First, the measurement precision (1σ) of geo-referenced wind was estimated at 0.07 m s^{-1}. Then, the effect of calibration parameter and aerodynamic characteristics of the UAV on wind measurement was examined by conducting a set of calibration flights. The results shown that the calibration improved the quality of measured wind field, and the influence of upwash and leverage effect can be ignored in wind measurement by the UAV. Third, for measurement of turbulent flux, the error caused by instrumental noise was estimated at 0.03 µmol m^{-2} s^{-1} for Fc, 0.02 W m^{-2} for H, and 0.08 W m^{-2} for LE. Fourth, data from the standard operational flights are used to assess the influence of resonance on the measurements and to test the sensitivity of the measurement under the variation (±30 %) of the calibration parameters around their optimum value. Results shown that the effect of resonance mainly affect the measurement of CO_2 (~5 %). The pitch offset angle (ε_θ) significantly affected the measurement of vertical wind (~30 %) and turbulent fluxes (~15 %). The heading offset angle (ε_ψ) mainly affected the measurement of horizontal wind (~15 %), and other calibration parameters had no significant effect on the measurements. The results lend confidence to use the UAV-based EC system, and suggest future improvements for optimization of the next generation system.

1 Introduction

In environmental, hydrological and climate change sciences, flux measurement at the regional scale (level of several to tens of kilometers) is a pressing problem (Mayer et al., 2022; Chandra et al., 2022). Process-based or remote sensing (RS)-based models are often used to estimate land surface fluxes of matter and energy at continental to global scales with typical spatial resolution from 1-10 km (Hu and Jia, 2015; Mohan et al., 2020; Liu et al., 1999). However, observational data, especially at similar scales to models' estimates, is often lacking, which presents a significant challenge for the validation and evaluation of the surface flux products from these models' estimates (Li et al., 2018; Li et al., 2017). On the ground, in the past decades, extensive eddy-covariance (EC) flux sites with their composed networks and optical-microwave scintillometer (OMS) sites have been built to provide temporally continuous monitoring of surface flux at local (hundreds of meters around the measurement site of ground EC) and path (a distance of a few hundred meters to near 10 kilometers between transmitter and receiver terminal of OMS) scales (Yang et al., 2017; Liu et al., 2018; Zhang et al., 2021; Zheng et al., 2023). However, flux from ground measurements need to be scaled up to kilometers-scale to provide comparable surface "relative-truth" flux data for the process- or RS-based models at larger spatial scales (Liu et al., 2016). But the spatial density of these flux measurements sites is still low compared to the heterogeneity of surface fluxes, which means that major scaling bias may exist in the upscaled flux data (Wang et al., 2016; Li et al., 2021). Therefore, regional-scaled oriented flux measurement techniques need to be developed to complement the missing scale between these ground- and models-based approaches (Chu et al., 2021).

Aircraft-based EC flux measurement method, which has been developed for turbulence measurements for more than 40 years (Lenschow et al., 1980; Desjardins et al., 1982), is considered as the optimum method to measure turbulent flux at regional scale (several hundred square kilometers) (Gioli et al., 2004; Garman et al., 2006). To date, several types of aircrafts, including manned or unmanned fixed-wing aircrafts, delta-wing aircrafts, and helicopters, have been used for measurements of turbulent flux by equipping them with the EC sensors to measure three-dimensional (3D) wind, air temperature, and gas concentrations at a high frequency (Gioli et al., 2006; Metzger et al., 2012; Wolfe et al., 2018; Sun et al., 2021a; Reuter et al., 2021). Among them, fixed-wing aircrafts and delta-wing aircrafts are better airborne platforms for EC measurements compared to helicopters due to their tightly coupled structure with the wind sensor and because their flow distortion around the fuselage can be more easily avoided or modeled (Prudden et al., 2018; Garman et al., 2008). A wide range of manned aircrafts has been developed to measure turbulent flux, including single-engine light aircrafts (e.g., Sky Arrow 650, Long-EC, WSMA) (Gioli et al., 2006; Crawford and Dobosy, 1992; Metzger et al., 2012), twin-engine aircrafts (e.g., Twin Otter, NASA CARAFE) (Desjardins et al., 2016; Wolfe et al., 2018) and larger quad-engine utility aircrafts (e.g., NOAA WP-3D) (Khelif et al., 1999). These airborne flux measurements, in combination with ground EC measurements, provide an excellent opportunity to produce regional-scaled, spatio-temporal continuous surface flux datasets that can improve our understanding of the processes of land-atmosphere interactions in regional and global change (Chen et al., 1999; Prueger et al., 2005; Calmer et al., 2019; Tadić et al., 2021). However, manned aircrafts are expensive to operate and maintain. Aviation safety and operational regulations require that manned aircrafts must fly above a minimum altitude (400 m above the highest elevation within 25 km on each side of the

center line of the air route in China) and must avoid hazardous conditions such as icing or severe turbulence. The flow distortion induced by the aircraft itself (from the wings, fuselage, and the propellers) complicates the wind vector measurement from aircraft platform, which means that sophisticated correction procedures should be applied to correct for the flow distortion effects (Elston et al., 2015; Williams and Marcotte, 2000; Drüe and Heinemann, 2013).

In recent years, interesting in unmanned aerial vehicle (UAV) platforms for atmospheric research have been fast growing, especially because of their lower construction, operation, and maintenance costs compared with manned platforms. High-performance fixed-wing UAVs offer a high payload capacity (5-10 kg) and similar endurance (2-3 h) and operating altitude (to 3500 m or higher above the sea level) to manned aircrafts, but with much less turbulence disturbance due to their small fuselage size (Reineman et al., 2013). More importantly, the advancements in small, fast, and powerful sensors and microprocessors make it possible to use of UAVs for comprehensive atmospheric measurements (Sun et al., 2021a). Several types of UAVs with different atmospheric measurement objectives have been developed and deployed, ranging from small size (e.g., 140 g SUMO) to medium (e.g., 1.5 kg M^2AV, 1.0 kg MASC) and large (e.g., 6.8 kg Manta, 5.6 kg ScanEagle) (Reuder et al., 2016; Båserud et al., 2016; Reineman et al., 2013; Zappa et al., 2020). A comprehensive overview of these UAVs for atmospheric measurement can be found in Elston et al. (2015) and Sun et al. (2021a). For turbulence measurement, the UAVs were equipped with a commercial or custom multi-hole (5- or 9-hole) probe paired with an integrated navigation system (INS) to obtain the wind vector. Small and medium UAVs typically could only measure fast 3D wind vector and air temperature fluctuations for measurements of momentum and sensible heat flux, whereas, large UAVs were equipped with more types (e.g., radiation, optics, or gas concentration) and more accurate sensors for measurement of more types of meteorological properties including sensible and latent heat fluxes, CO_2 flux, radiation fluxes as well as surface properties (Reineman et al., 2013; Sun et al., 2021a). UAVs can be deployed in a variety of application environments and complex conditions, which offer distinct advantages over manned aircraft in their ability to safely perform measurements in low-altitude conditions (below 100 m above the ground level) and greatly reduce operational costs (Witte et al., 2017). Anderson and Gaston (2013) predict that UAVs will revolutionize the spatial data collection in ecology and meteorology.

EC method is a well-developed technology for directly measuring vertical turbulent flux (flux of sensible heat, latent heat and CO_2) within the atmospheric boundary layers (ABL) (Peltola et al., 2021). It requires accurate time (for ground tower) or spatial (for mobile platform) series of both the transported scalar quantity and the transporting turbulent wind. Each should be measured at sufficient frequency to resolve the flux contribution from small eddies (Vellinga et al., 2013). However, the measurement of the geo-referenced 3D wind vector, which is the prerequisite for EC measurements, is challenging for airborne platform. The geo-referenced 3D wind measured by airborne is the vector sum between the aircraft velocity relative to the earth (inertial velocity) and the velocity relative to the air (relative wind vector, or true airspeed). Therefore, accurate measurements of the relative wind as well as the motion and attitude of the platform are essential to accurately measure the geo-referenced wind vector and the turbulent flux (Metzger et al., 2011). Garman et al. (2006) estimated the measurement precision (1σ) of the vertical wind measurements of a commercial 9-hole turbulence probe (known as "Best Air Turbulence Probe", often abbreviated as the "BAT Probe") to be 0.03 m s^{-1} by combining the precision of the BAT Probe and the integrated

100 navigation system. A light delta-wing EC flux measurement aircraft developed by Metzger et al. (2011) reported a 1σ precision

101 of wind measurement of 0.09 m s^{-1} for horizontal wind and 0.04 m s^{-1} for vertical wind using a specially customized five-hole

102 probe (5HP). On this basis, in combination with a commercial infrared gas analyzer, the 1σ precision of flux measurement

103 was 0.003 m s^{-1} for friction velocity, 0.9 W m^{-2} for sensible heat flux, and 0.5 W m^{-2} for latent heat flux (Metzger et al., 2012).

104 The EC flux measurement from a UAV platform can now be achieved with a similar reliability to a manned platform. The

105 Manta and ScanEagle UAV-based EC measurements developed by Reineman et al. (2013) achieved precise wind

106 measurements (0.05 m s^{-1} for horizontal and 0.02 m s^{-1} for vertical wind) using a custom nine-hole probe and a commercial

107 high precision integrated navigation system (INS). However, the onboard instrument packages for Manta and ScanEagle UAV

108 are independent of each other in their measurements of turbulent and radiation flux, and the CO_2 flux measurement is lacking.

109 Inspired by these studies, Sun et al. (2021a) used a high-performance fuel-powered vertical take-off and landing (VTOL)

110 fixed-wing UAV platform to integrate the scientific payloads for EC and radiation measurements to obtain a comprehensive

111 measurement of turbulent and radiation flux. This UAV-based EC system could measure turbulent fluxes of sensible heat,

112 latent heat, and CO_2, as well as radiation fluxes including net radiation and upward- and downward-looking photosynthetically

113 active radiation (PAR). This system was successfully tested in the Inner Mongolia of China and applied to measure the regional

114 sensible and latent heat fluxes in the Yancheng coastal wetland in Jiangsu, China (Sun et al., 2021a; 2021b). During these field

115 studies, the UAV-based EC measurements achieved a near consistent observational result compared with ground EC

116 measurements (Sun et al., 2021b). However, some shortcomings in the developed UAV-based EC system were also identified.

117 In particular, the noise effects from the engine and propeller were not fully isolated, resulting in high frequency noise in the

118 measured scalars (air temperature, H_2O, and CO_2 concentration). This UAV-based EC system is being continuously improved

119 (in Section 2.1). However, no quantitative evaluation of the measurement precision of the wind field and turbulent flux as well

120 as of the influence of the resonance noise from the UAV operation have been made yet. Previous work using ground EC as a

121 benchmark to assess the measurement performance of the UAV-based EC system has been disputed, due to difference in EC

122 sensors, platforms, measurement height, and source areas (i.e., footprint), as well as the influence of surface heterogeneity,

123 flux divergence, inversion layer and the stochastic nature of turbulence (Sun et al., 2021b; Wolfe et al., 2018; Hannun et al.,

124 2020).

125 This study attempts to evaluate the performance of the UAV-based EC system developed by Sun et al. (2021a) in the

126 measurement of wind field and turbulent flux. For these purposes, data from two field measurement campaigns, including a

127 set of calibration flights and some standard operation flights, were used in this study. First, the current study investigated the

128 quality of the measurement of geo-referenced wind vector including measurement error (1σ) and the improvements for wind

129 measurement after system calibration. Second, using the measured data from standard operation flights, flux measurement

130 error related to instrumental noise was estimated with a method proposed by Billesbach (2011). Errors propagated through the

131 correction terms [i.e., Webb-Pearman-Leuning (WPL) correction for latent heat and CO_2 flux] were also included in our

132 analysis (Webb et al., 1980; Kowalski et al., 2021). Then, the impacts of resonance noise on the measured scalar variance and

133 the flux covariance were also estimated by comparing the real (co)spectra curve with the theoretical reference curve from

134   Massman and Clement (2005). Lastly, the sensitivity of the measured geo-referenced wind vector and turbulent flux to the

135   errors in the calibration parameters (determined by the calibration flight) were assessed by adding an error of ±30 % to their

136   calibrated value.

137   2 Materials and Methods

138   2.1 The UAV-based EC system

139   The VTOL fixed-wing UAV platform used for EC measurement has minimal requirements for the takeoff location and offers

140   a high payload capacity of up to 10 kg. This UAV has a wing-span of 3.7 m, a fuselage length of 2.85 m, and a maximum take-

141   off weight of 60 kg. The UAV engine is mounted in a pusher configuration, allowing for the turbulence probe to be installed

142   directly on the nose of the UAV, minimizing or eliminating airflow contamination due to upwash and sidewash generated by

143   the wings (Crawford et al., 1996). Control of the UAV is totally autonomous, and the pilots have the option to enable manual

144   control in emergency conditions. The UAV has a cruise flight speed of 28 to 31 m s^{-1} with an endurance of almost 3 h, and it

145   has a flight ceiling of up to 3800 m above the sea level. Detailed information about this UAV could be found in Sun et al.

146   (2021a).

147   The flux payloads of the UAV-based EC system include a precision-engineered 5-hole pressure probe (5HP) for

148   measurement of the true airspeed and the attack (α) and sideslip (β) angles of the incoming flow relative to the UAV, a dual-

149   antenna integrated navigation system (INS) for high accuracy measurement of UAV ground speed and attitude, an open path

150   infrared gas analyzer (IRGA) for recording the gas concentrations of CO_2 and water vapor, a fast temperature sensor for

151   measurement of the fast temperature fluctuations, and a slow-response temperature probe for providing a mean air temperature

152   reference. The sensor modules and their 1σ precision of the measured variables related to EC measurement were listed in

153   Table 1. For the 5HP, the 1σ measurement precision was acquired from the wind tunnel test after wind tunnel calibration (Sun

154   et al., 2021a).

155   **Table 1**: Summary of the sensor modules, measured variables, and their measurement precision used to determine the geo-

156   referenced wind velocity and turbulent flux.

Sensor (Module, company, country)	Variables	Precision (1σ)
GNSS/INS (BD992-INS, Trimble, USA)	Roll, Pitch, Heading	0.1º
	Horizontal velocity	0.007 m s^{-1}
	Vertical velocity	0.02 m s^{-1}
5HP (ADP-55, Simtec AG, Switzerland)	Attack angle	0.02º[#]
	Sideslip angle	0.04º[#]
	True airspeed	0.05 m s^{-1}[#]
	Static pressure	1.1 hPa
	Dynamic pressure	0.003 hPa
IRGA	CO_2 density	0.2 mg m^{-3}

(EC150, Campbell, USA)	H$_2$O density	0.004 g m^{-3}
Thermistor (100K6A1IA, Campbell, USA)	Temperature (slow)	0.2 ℃
Thermocouple (T-type COCO-003, Omega, USA)	Temperature (fast)	0.5 ℃

157 [#] Results from the wind tunnel test.

158   The sample rate of EC measurement is 50 Hz except for the slow-response temperature probe (1 Hz), yielding a turbulence

159 horizontal resolution of approximately 1.2 m at a cruising speed of 30 m s^{-1}. The system was improved according to deficiencies

160 identified after several field measurements with the following adjustments: 1) a laser distance measurement unit was mounted

161 for measuring the distance between the UAV and the ground level, 2) the platinum resistance thermometer was replaced by a

162 thermocouple (Omega T-type COCO-003; Ø0.075 mm) for improving the resistance of the high-frequency temperature

163 measurements to vibration noise from the engine, 3) the vibration isolator structure of the IRGA was improved, and 4) the

164 original datalogger (CR1000X, Campbell, USA) was replaced with a lighter one (CR6, Campbell, USA). All the digital and

165 analog signals from the sensor modules are stored and synchronized by the on-board datalogger, and the on-board scientific

166 payloads are designed to be isolated from the electronic components of the UAV to ensure that any problems occurring would

167 not jeopardize the safety of flying (Sun et al., 2021a).

2.2 Field campaign

2.2.1 In-flight calibration campaign

170 In order to calibrate the mounting error in 5HP of the UAV-based EC system, an in-flight calibration campaign was carried

171 out on 4 September 2022 at the Caofeidian Shoal Harbor in the Bohai Sea of northern China. At low tide, a large area of the

172 tidal flat is exposed; while at high tide, only the barrier islands are visible (Xu et al., 2021). The assumption conditions should

173 be satisfied for calibration flight including 1) low turbulent transport condition (i.e., no disturbance), 2) a constant mean

174 horizontal wind, and 3) mean vertical wind near zero (Drüe and Heinemann, 2013; Vellinga et al., 2013; Van Den Kroonenberg

175 et al., 2008). This allows identical wind components for several consecutive straights in opposite or vertical flight directions.

176 These assumptions are usually well satisfied above the ABL or under stable atmospheric conditions (Drüe and Heinemann,

177 2013). Over the sea surface, due to its uniform and cool surface property, the turbulence fluctuations are weaker than that over

178 the land surface (Mathez and Smerdon, 2018), making where a more ideal environment to conduct calibration flight.

179   The in-flight calibration campaign in this study included three flight maneuvers: 'box' maneuver, 'racetrack' maneuver, and

180 'acceleration-deceleration' maneuver. The trajectories of these flight maneuver are shown in Figure 1. The calibration flight

181 was executed between 7:28 a.m. and 7:48 a.m. (Beijing time), and the averaged flight altitude was 400 m ($\sigma = \pm 0.78$ m)

182 above the sea level. Considering the uniform and cool underlying surface and the stable atmospheric conditions of the early

183 morning, we assume no disturbance from the underlying surface during the calibration flight and the assumptions for

184 calibration flight are satisfied.

185
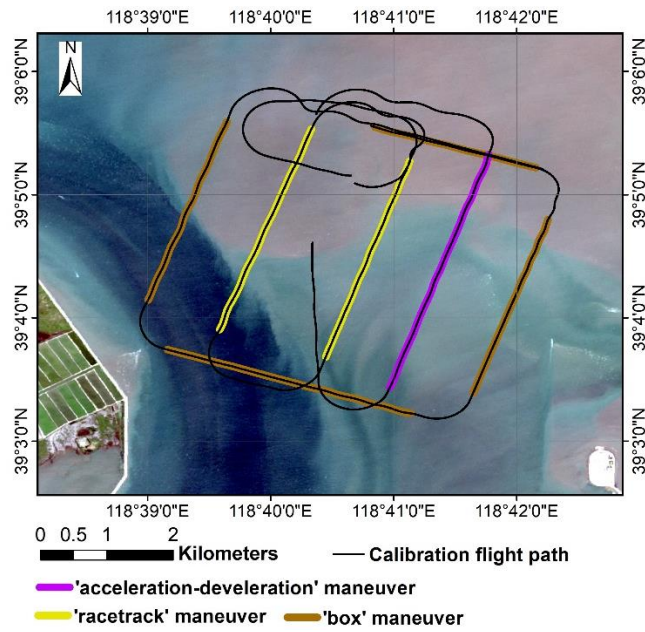
Figure 1. Flight trajectories of the calibration flight campaign carried out on 4 September 2022 at the Caofeidian Shoal Harbor in the Bohai Sea of northern China. The land surface image is from Sentinel-2A satellite image with true color combination acquired on 1 September 2022.

189   The 'box' maneuver (gray line in Fig. 1) is used to determine the mounting misalignment angle in the heading (ϵ_ψ) and

190   pitch (ϵ_θ) between the 5HP and the center of gravity (CG) of the UAV. The flight path is a box in which the four straight legs

191   are flown at constant cruising speed, flight altitude, and heading continuous for 2 minutes. The 'racetrack' maneuver (yellow

192   line in Fig. 1) is used to evaluate the quality of the calibration parameters acquired from the previous 'box' maneuver. The

193   flight path consists of two parallel straight flight tracks connected by one 180° turns. Each straight flight section lasts 2 minutes

194   at constant speed and flight altitude. Lastly, the 'acceleration-deceleration' maneuver (purple line in Fig. 1) is used to check

195   the influence of lift-induced upwash from the wing to the measured attack angle by the 5HP. During this maneuver, the aircraft

196   is kept straight and level at constant pressure altitude. When beginning this maneuver, the aircraft accelerates to its maximum

197   airspeed (35 m s^{-1}). Then, the airspeed reduces gradually to near its minimum airspeed (25 m s^{-1}) and back up to its maximum

198   airspeed. The pressure-altitude of the aircraft is maintained throughout this maneuver, and the entire maneuver lasts one minute.

199   This maneuver creates a series continuous changed pitch (θ) and attack (α) angle. If a relationship between the measured

200   incident flow attack angles (α) by the 5HP and the measured pitch angle by the INS close to 1:1, then it indicates that the effect

201   from the fuselage-induced flow distortion on the wind measurements is negligible (Garman et al., 2006).

202   **2.2.2 Standard operation flight campaign**

203   The reliability of the EC measurement from UAV is susceptible to several factors, mainly including instrumental noise,

204   resonance noise, and the quality of the calibration parameter, etc. In order to evaluate the flux measurement error related to

205 instrumental noise, the effects of resonance on the measured scalar and to investigate the sensitivity of the measured geo-

206 referenced wind vector and turbulent flux to uncertainty in the calibration parameter, we used data from 7 flights in the Dagang

207 district in Tianjin, China between 8 and 16 August 2022. This area is located on the west coast of the Bohai Sea and is a coastal

208 alluvial plain with altitudes between 1-3 m (Chen et al., 2017). The flight path, shown in Figure 2, includes three parallel

209 transect lines of approximately 4 km in length each and at 1-2 km intervals. All flights occurred during the daytime, and were

210 performed in the same trajectory at a low altitude about 90 m above sea level. The flight area covered three different underlying

211 surface types: land, coastal zone, and water surfaces, that can represent typical flux intensity characteristics over different

212 surface conditions.

213
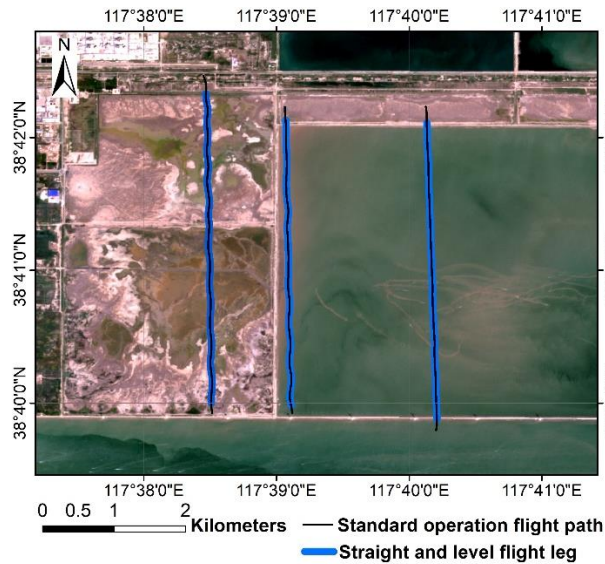
Figure 2. Flight trajectories of the standard operation flight campaign carried out between 8 and 16 August 2022 at Dagang district, Tianjin, China. The land surface image is from Sentinel-2A satellite image with true color combination acquired on 27 August 2022.

216 During the standard operation flight campaign, the atmospheric stability changed from the stable (Monin-Obukhov stability

217 parameter, $z/L = 1.93$) to very unstable ($z/L = -10.28$) conditions as measured by the UAV, where z is the flight height

218 above the ground level, L is the Obukhov length. The stable condition mostly occurred on flight path located over the sea

219 surface, while the unstable condition mostly occurred on flight path located over the land surface. These flight data provided

220 various measurement conditions for us to evaluate the performance of the developed UAV-based EC system.

221 **2.3 Data processing**

222 The raw data collected with the on-board datalogger (CR6, Campbell, USA) is subsequently saved in Network Common Data

223 Form (netCDF) format. It includes dynamic and static pressure, attack, and sideslip angle of incoming flow; slow (1 Hz) and

224 fast (50 Hz) air temperature; mass concentration of H_2O and CO_2; as well as the full navigation data (including 3D location,

225 ground speed, angular velocity, and attitude, etc.) of the UAV. The subsequent data processing includes three stages in order

226 to calculate flux data from raw measured data.

227   In the first stage, a moving average filter was used to detect outliers in each variable. Detected outliers were removed and

228 replaced by values obtained by linear interpolation. Outliers tend to be rare. However, if outliers constitute more than 20 % of

229 the data points, the corresponding flight data should be discarded.

230   In the second stage, geo-referenced 3D wind vector is calculated. The full form of the equations for calculating the geo-

231 referenced wind vector by the UAV-based EC system is described in detailed in Supplement Part A. From the airborne platform,

232 geo-referenced wind vector is measured in two independent reference coordinate systems: the relative true airspeed ($\widehat{U}_a$)

233 measurement in the aircraft coordinate system and the ground speed of the aircraft (U_p) in the geo-referenced coordinate

234 system. The geo-referenced wind (U) is the vector sum of the relative true airspeed ($\widehat{U}_a$), the UAV's motion (U_p) and the

235 tangential velocity due to the rotational motion of the aircraft ("lever arm" effect), which is described in Eq. (S2). In this stage,

236 the acquired calibration parameters (ϵ_ψ and ϵ_θ) from the calibration flight are substituted into the Eq. (S8) to correct the

237 mounting angle offset errors between the 5HP and the CG of the UAV. The final equations for geo-referenced wind vector

238 calculation (Eqs. S15 to S17) revealed that the lever arm effects due to the spatial separation between the tip of the wind probe

239 and the CG of UAV may influence the wind measurements. Typically, the separation distance (L) is small, and the influence

240 of the lever arm effects can be ignored when the L is less than about 10 m (Lenschow, 1986). In the current UAV-based EC

241 system, the displacements of the 5HP tip with respect to the CG of the UAV along the three axes of UAB body coordinate are:

242 $x^b = 1.459$ m, $y^b = 0$ m, and $z^b = 0.173$ m (in Supplement Part A). Therefore, in practice, the influence of leverage effects

243 in geo-referenced wind calculation was also ignored in this study. This was also confirmed by assessing the difference in the

244 geo-referenced wind vector with and without the leverage effect correction term in this study (in Section 3.1).

245   In the final stage, based on the EC technology and spatial averaging, turbulent fluxes are calculated using the covariances

246 of vertical wind (w) with air temperature (T_a) for sensible heat flux (H), with water vapor density (q) for latent heat flux (LE),

247 and with CO_2 density (c) for CO_2 flux (F_c), and with the necessary correction (Webb et al., 1980). The time lag due to the

248 separation between the 5HP tip, the adjacent temperature probe, and the open-path gas analysis did not need to be corrected

249 because the time delay was very small at the cruise airspeed of 30 m s^{-1} and sensor separation less than 20 cm. Only the

250 measurement data from the straight-line portion of the flight path was used in flux calculation. Detailed calculation procedure

251 and formulas for calculating H, LE, and F_c used by the current UAV-based EC system are provided in Supplement Part B,

252 including spatially averaging, coordinate rotation, and necessary correction (i.e., WPL correction for LE and F_c). In this study,

253 the entire measured data of each straight and level flight leg (each with length about 4 km) from the standard operational flight

254 campaign was used to calculate turbulent flux, regardless of the uncertainty in fluxes associated with spatial averaging.

2.4 Evaluation scheme

2.4.1 Wind measurement evaluation

The key to successful aircraft EC measurements lies in the translation of accurately measured, aircraft-orientated, wind vector to geo-referenced orthogonal wind vector (Thomas et al., 2012). Determining the geo-referenced wind vector requires a sequence of thermodynamic and trigonometric equations (Metzger et al., 2012), these equations propagate various sources of error to the measured geo-referenced wind vector. To estimate the measurement errors in the geo-referenced wind vector, we used the linearized Taylor series expansions of Eqs. (S15) to (S17) derived by Enriquez and Friehe (1995) (Eqs. S18 to S20 in Supplement Part A) to determine the sensitivities of each of the geo-referenced wind vector components with respect to the relevant variables. Then, these sensitivity terms can be combined to compute the overall measurement error (1σ) in the geo-referenced 3D wind vector (Eqs. S21 to S23 in Supplement Part A).

The above wind measurement error analysis gives the nominal measurement precision of the geo-referenced wind, but does not consider the influence of environmental changes. Following the methods of Lenschow and Sun (2007), we assess whether the accuracy of wind measurements from the UAV in satisfying the minimum signal level needed for resolving the mesoscale variations of the three wind components in the encountered atmospheric conditions. Firstly, the minimum required signal level for measurement of vertical air speed (ω) under the encountered atmospheric conditions could be estimated as (Lenschow and Sun, 2007):

$$\frac{\partial w}{\partial t} < 0.2\sqrt{2}\sigma_w 2\pi k U_a \tag{1}$$

with the true airspeed (U_a) set to mean cruise speed 30 m s^{-1}, σ_w is the peak signal magnitude of the power spectra, and k is the corresponding wavenumber (Thomas et al., 2012). The measurement error in the vertical wind component can be calculated as (Lenschow and Sun, 2007):

$$\frac{\partial w}{\partial t} \cong \Theta \frac{\partial U_a}{\partial t} + U_a \frac{\partial \Theta}{\partial t} + \frac{\partial w_{UAV}}{\partial t} \tag{2}$$

with $\Theta = \alpha - \theta$, where α is the attack angle, θ is the pitch angle, w_{UAV} is the UAV's vertical velocity. According to Lenschow and Sun (2007), the signal level and mesoscale fluctuation of horizontal wind components (u and v) are considerably larger than that of vertical wind, so the accuracy criteria are not nearly as stringent. The measurement error of the horizontal wind component could be calculated as (Lenschow and Sun, 2007):

$$\frac{\partial u}{\partial t} \cong -\frac{\partial U_a}{\partial t} + \frac{\partial u_{UAV}}{\partial t} \tag{3}$$

$$\frac{\partial v}{\partial t} \cong \Psi \frac{\partial U_a}{\partial t} + v_{tas} \frac{\partial \Psi}{\partial t} + \frac{\partial v_{UAV}}{\partial t} \tag{4}$$

and,

$$\Psi \equiv \psi' + \beta \tag{5}$$

284   where u_{UAV}, v_{UAV} are the UAV's horizontal velocity measured from INS, ψ' is the departure of the measured true heading

285   from the average true heading, and β is the sideslip angle of airflow. If the measurement error of the 3D wind vector from Eqs.

286   (2) to (4) is smaller than the required minimum signal level of the vertical and horizontal wind components, it can be confirmed

287   that the measurement accuracy of the geo-referenced 3D wind vector from UAV is sufficient to resolve the mesoscale

288   variations of the three wind components in the encountered atmospheric conditions.

289   In addition, accurate measurements of geo-referenced wind vector typically not only depend on the measurement precision

290   of the sensors (i.e., 5HP and INS), but also related to the quality of the calibration parameters and the geometry structure of

291   the UAV (i.e., flow distortion and leverage effect). For evaluation of the effect of the latter two, a calibration flight campaign

292   (Section 2.2.1) was performed to determine the calibration parameter ($\epsilon_\psi, \epsilon_\theta$), check its quality, as well as to ascertain the

293   effects of the lever arm and up-wash by the wings. The methods for acquiring the calibration parameter were given by Vellinga

294   et al. (2013) and Sun et al. (2021a), and the results are reported in Supplement Part C (Figs. S2 and S3). During the in-flight

295   calibration campaign, a 'racetrack' maneuver was performed to check the quality of the calibration parameters determined

296   from the 'box' flight maneuver. The initial ($\epsilon_\psi = 0°, \epsilon_\theta = 0°$) and calibrated ($\epsilon_\theta = -0.183°, \epsilon_\psi = 2°$, in Supplement Part C)

297   set of parameters were used to calculate the geo-referenced wind vector. By comparing the mean and standard deviation of the

298   horizontal and vertical wind vector between the initial and calibrated set, the quality of the geo-referenced wind vector

299   measurement in real environment conditions can be verified.

300   The relative wind vector ($\widehat{U}_a$) measured by the aircraft is susceptible to flow distortion because the airplane must distort the

301   flow to generate lift and thrust. The aircraft's propellers, fuselage, and wings are the main sources of flow distortion as flow

302   barriers (Metzger et al., 2011). For fixed-wing aircrafts, the wind probe mounted on the nose of the UAV and extended as far

303   forward of the fuselage as possible could avoid the flow distortion induced by the fuselage and propellers. Effects from the

304   induced upwash by the wings can also influence the correspondence between the measured and free-stream flow variables

305   (Garman et al., 2008). The induced upwash modifies the local angle of attack, causing the measured attack angle (α) to be

306   larger than the free-stream attack angle (α_∞)(Garman et al., 2008). Therefore, for wind measurements by large-scale manned

307   fixed-wing aircrafts, the upwash effects must be corrected (Garman et al., 2008; Kalogiros and Wang, 2002). However, UAV

308   seldom need this correction due to the fuselage size and the airspeed is very low compared to a manned aircraft.

309   In this study, in order to access whether the lift-induced upwash could be safety ignored by the current UAV-based EC

310   system, an 'acceleration-deceleration' flight maneuver was performed. According to Crawford et al. (1996), the pitch angle

311   (θ) by the INS instrument can be utilized as an estimate of the free-stream attack angle (α_∞) if the aircraft's vertical velocity

312   is zero, since it is unaffected by lift-induced upwash and varies directly with α_∞ when the ambient vertical wind is zero. Under

313   ideal conditions (zero aircraft vertical velocity and zero ambient vertical wind), the approximation relationship of $\theta \cong \alpha_\infty$ is

314   valid when $\theta < 6°$ (Crawford et al., 1996; Vellinga et al., 2013). Departures from the 1:1 relationship can be caused by airflow

315   distortion around the airplane behind the 5HP. The 'acceleration-deceleration' maneuver produced various pitch and attack

316   angles measured under various airspeeds, which allowed a direct comparison between the pitch angle (θ) and the attack angle

317 (α). If the slope between α and θ is close to unity, it indicates that the influence of lift-induced upwash can be ignored;

318 otherwise, its influence should be corrected (Garman et al., 2006). Meanwhile, the influence of leverage effects was also

319 evaluated based on the measurement data from the 'acceleration-deceleration' maneuver by considering or ignoring the

320 leverage effect correction term in Eqs. (S15) to (S17).

2.4.2 Flux measurement error caused by instrumental noise

322 Flux measurement error from UAV can be attributed to several sources, mainly including instrumental noise, data handing,

323 atmospheric conditions, spatial averaging length, and bumpy flight environment (Mahrt, 1998; Finkelstein and Sims, 2001;

324 Mauder et al., 2013). They can be systematic or random. Determination of the flux measurement error caused by instrument

325 noise is very useful, as it is related not only to the system performance, but also to the minimum resolvable capability for the

326 flux to be measured. In the current study, uncertainty related to instrumental noise (listed in Table 1) was estimated using the

327 directly method proposed by Billesbach (2011). This method can be called as "random shuffle" (denoted as the RS) method

328 and was "designed to only be sensitive to random instrument noise". According to Billesbach (2011), the uncertainty of the

329 flux covariance can be expressed as:

330 $\sigma_{\overline{w'x'}} = \frac{1}{N} \sum_{i,j=1}^{N} w'(t_i) x'(t_j)$ (6)

331 where x is the target entity of the covariance, N is the number of measurements contained in the block averaging period, $j \in$

332 $[1 \dots N]$ but the values are in the random order. The idea behind the RS method was that the randomly shuffled will remove

333 the covariance between biophysical (source/sink) and transport mechanisms, leaving only the random "accidental" correlations

334 attributed mostly to instrument noise (Billesbach, 2011). It means that the shuffled component x makes it uncorrelated in

335 time/space and decorrelates x from w, resulting in two independent variables (i.e., $\overline{w'x'} \sim 0$), and any residual value (i.e.,

336 $\overline{w'x'} \neq 0$) of the covariance is attributed to random instrument noise.

337   In this study, in order to obtain a robust estimate of the instrumental noise, $\sigma_{\overline{w'x'}}$ was repeatedly calculated 20 times for every

338 straight and level flight leg in operation flight (Fig. 2), and the mean of the absolute values of these repeated estimated $\sigma_{\overline{w'x'}}$

339 were used to estimate the random uncertainty related to instrumental noise. According to Rannik et al. (2016), RS method

340 tends to overestimate the covariance uncertainty. Then, the uncertainty in the flux covariance of sensible heat ($\sigma_{\overline{w'T'}}$), latent

341 heat ($\sigma_{\overline{w'\rho'_v}}$), and CO_2 ($\sigma_{\overline{w'\rho'_c}}$) were estimated using RS method, respectively.

342   It should be noted that the measurement error of EC flux is influenced not only by the uncertainty in the raw covariance but

343 also by the propagated errors form the correction terms (i.e., WPL correction) or any lens contamination (Serrano-Ortiz et al.,

344 2008). The signal quality of the IRGA was checked before each flight measurement to ensure that the measurement of gas

345 concentration is not affected by lens contamination. The relative uncertainty of flux measurement was estimated using the

346 partial derivatives of the flux calculation equation derived by Liu et al. (2006) (Eqs. S28 to S30 in Supplement Part B). These

347 equations ignored the perturbations terms from the errors in the individual scalar (i.e., ρ_v, ρ_c, T) which were proved very small

348 (Serrano-Ortiz et al., 2008). At last, after several repetitive calculation of the Eq. (6), their averaged value then be combined

349 to Eqs. (S28) to (S30) for estimating the flux measurement error caused by instrumental noise.

2.4.3 Resonance effects

351 Previous work found that the measurement of the atmospheric scalars (e.g., air temperature, H_2O, and CO_2 concentration) by

352 the current UAV-based EC system were susceptible to resonance effects caused by the operation of the engine and propeller

353 (Sun et al., 2021b). In order to further reduce the noise influence from resonance effects, the vibration damping structure was

354 further optimized. Then, the reference (co)spectra curve of Massman and Clement (2005) was used to quantify the influence

355 of the resonance effects remaining after vibration isolation optimization. Massman and Clement (2005) gave the generalization

356 mathematical expression of the models of spectra and co-spectra:

357
$$Co(f) = A_0 \frac{1/f_x}{[1+m(f/f_x)^{2\mu}]^{\frac{1}{2\mu}(\frac{m+1}{m})}} \tag{7}$$

358 where f is frequency (Hz), f_x is the frequency at where $fCo(f)$ reaches its maximum value, A_0 is a normalization parameter,

359 m is the (inertial subrange) slope parameter, and μ is the broadness parameter. To describe co-spectra, m should be 3/4; to

360 describe spectra, m should be 3/2. According to Massman and Clement (2005), μ was set to 7/6 under stable atmospheric

361 condition and was set to 1/2 under unstable atmospheric condition. Fast Fourier transform (FFT) method was used to calculate

362 the spectra and co-spectra of the measured turbulent variables. Before calculating the turbulence (co)spectra, condition of the

363 raw turbulence data was performed, including linear detrend and tapering using the Hamming window to reduce the spectral

364 leakage (sharp edge) according to Kaimal et al. (1989).

365 The noise influence from resonance mainly appears in the high frequency domain. According to the feature of spectral curve,

366 the frequency range of the noise region was artificially designated to $f > 8$ Hz for air temperature, $f = 1\sim5$ Hz for water

367 vapor, and $f = 1\sim8$ Hz for CO_2. The normalized spectra and co-spectra curve were adopted and the area difference of the

368 designated frequency range beneath the (co)spectra curve between the measured and reference (co)spectra curve was calculated

369 to quantify the influence of resonance noise in the variance and flux covariance of the measurement atmosphere scalars. An

370 example is shown in Figure 3, and also shown the reference (co)spectra curve of Massman and Clement (2005), with the

371 (co)spectral maximum at $f_x = 0.1$. The red region in Fig. 3 represented the impact extent of the resonance noise in the variance

372 (Figs. 3a to 3c) and flux covariance (Figs. 3d to 3f) of the measured scalars.
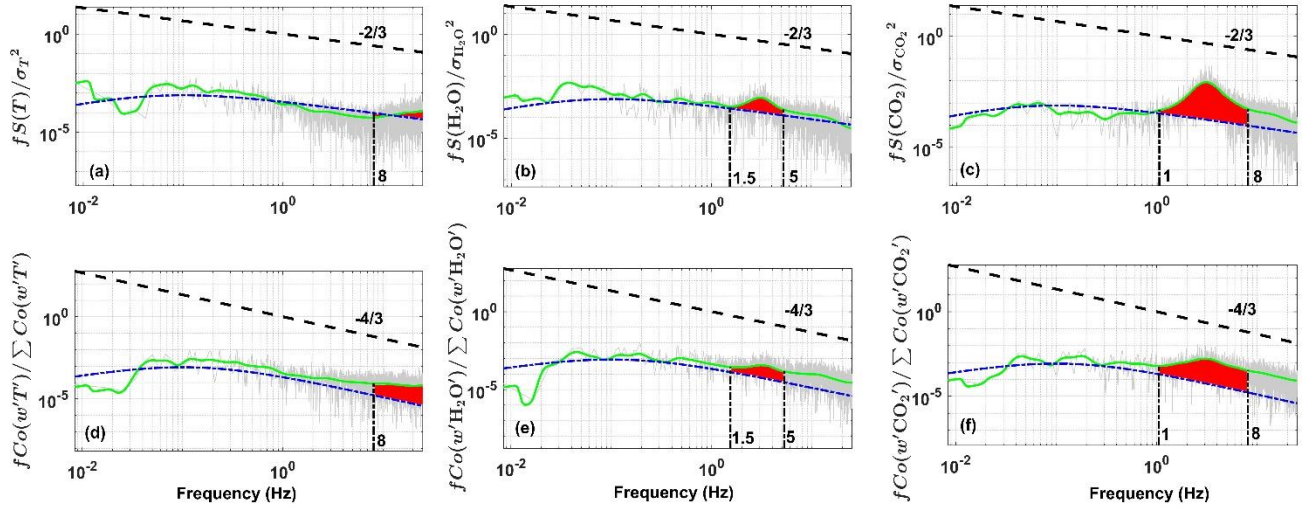
Figure 3. Influence of the resonance noise on the spectra (top row) and co-spectra (bottom row) curve of the measured scalars based on the measured data from one standard operation flight carried out on 8 August 2022 at Dagang district, Tianjin, China. The red region is the area difference of the designated frequency range (vertical black dashed-dotted line) beneath the (co)spectral curve between the measured and reference (co)spectral curve.

2.4.4 Sensitivity analysis

To understand the relevance of the calibration parameters for the measurement of geo-referenced wind vector and turbulent flux, two sensitivity tests were conducted. The magnitude of the perturbation in the wind vector and turbulent flux was investigated as a function of the uncertainties in the four calibration parameters, including three mounting misalignment angles ($\epsilon_\psi, \epsilon_\theta, \epsilon_\phi$) between the 5HP and the CG of the UAV and one temperature recover factor ($\epsilon_r = 0.82$) used to calculate the ambient temperature (Eq. 3 in Sun et al. 2021a).

First, the sensitivity of the geo-referenced wind vector and turbulent flux to the uncertainties in the individual calibration parameter was investigated. The geo-referenced wind vector and turbulent flux were calculated based on the straight leg (about 4 km) of the standard operational flight by adding an error of ± 30 % to the calibrated value of each calibration parameter alternately; except for ϵ_ϕ, for which the typical range of $\pm 0.9°$ was taken for sensitivity analysis (Vellinga et al., 2013).

Then, in order to test the overall interaction between the parameters, a second sensitivity test was performed to calculate the geo-referenced wind vector and turbulent fluxes by adding ± 30 % error to all calibration parameters simultaneously. Lastly, their relative errors (*RE*) with respect to the original value were calculated to evaluate the perturbation of the wind vector and turbulent flux under the variation of each calibration parameter as well as under simultaneous variation of all calibration parameters. In the sensitivity analysis, the calculated geo-referenced wind and turbulent flux whose absolute value was less than their least resolvable magnitude were filtered out to avoid the influence of the errors contained in the measurements themselves on the results.

395 **2.4.5 Relative error**

396 In this study, relative error (*RE*) was used to evaluate the influence of different factors on the measurements of geo-referenced

397 wind vector and turbulent flux. It is defined as:

398 $RE = \frac{|x_0| - |x|}{|x|} \times 100\ \%$ (7)

399 where '| |' means the absolute value, x is the 'true' value, x_0 is the influenced value. $RE > 0$ means the exerted influence will

400 cause the measurement value to be larger than 'true' value and vice versa.

401 **3 Results**

402 **3.1 Wind measurement evaluation**

403 Wind measurement evaluation for the UAV-based EC system includes three contents: (1) measurement precision and its ability

404 to resolve the mesoscale variations of the wind, (2) checking the quality of the acquired calibration parameters, and (3)

405 checking whether the measured wind vector is affected by upwash flow and leverage effects.

406 First, according to the equations described in Supplement Part A (Eqs. S18 to S23), the measurement precision of horizontal

407 wind components is a function of true airspeed and true heading, while, the measurement precision of vertical wind component

408 is largely decided by the true airspeed. The typical values of true airspeed ranging from 25 m s^{-1} to 35 m s^{-1} (interval of 1 m s^{-}

409 ^{1}) and the true heading values ranging from 0° to 180° (interval of 30°) were used in the evaluation of wind measurement

410 error. Then, the measurement precision (1σ) of the geo-reference 3D wind vector from aircraft was estimated using the

411 measurement precision of the related parameters from Table 1. The results are shown in Figure 4 for the measurement precision

412 of horizontal wind (σ_u and σ_v in Figs. 4a and 4b) and vertical wind (σ_w in Fig 4c), respectively. The typical values of the

413 measurement precision are ranging from 0.05 m s^{-1} to 0.07 m s^{-1} for horizontal wind component u, ranging from 0.02 m s^{-1} to

414 0.08 m s^{-1} for horizontal wind component v, and ranging from 0.05 m s^{-1} to 0.07 m s^{-1} for vertical wind component w.
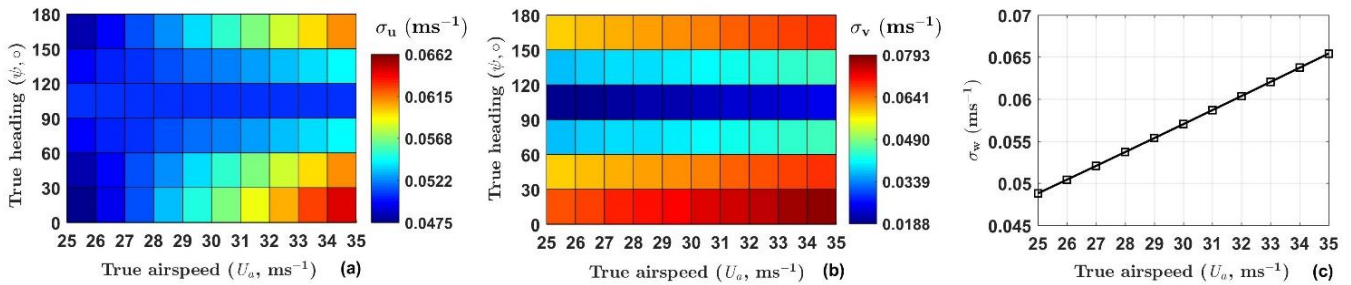
415

416 **Figure 4. Estimated measurement precision (1σ) of the horizontal wind (a, b) and vertical wind (c) according to the equations**
417 **described in Supplement Part A (Eqs. S18 to S23).**

418 Generally speaking, an autopiloted UAV can maintain a near-constant true airspeed during the cruise flight phase. At a true

419 airspeed of 30 m s^{-1} for the current UAV during the cruising, the maximum measurement error in the northward, eastward, and

vertical velocities of the geo-referenced wind components were calculated as approximately 0.06, 0.07, and 0.06 m s^{-1}, respectively. Then, we assume that a minimum signal-to-noise ratio of 10:1 is required to measure the wind components with sufficient precision for EC measurement (Metzger et al., 2012). Accordingly, in the real environments, horizontal and vertical wind speed greater than 0.7 m s^{-1} and 0.6 m s^{-1} can be reliably measured, respectively (Table 2).

Table 2: The maximum measurement error in the northward (u), eastward (v), and vertical (w) velocities of the geo-referenced wind components at the true airspeed of 30 m s^{-1}, and the least resolvable magnitude assuming the minimum required signal-to-noise ratio of 10:1.

Measurements	Measurement precision (1σ)	Least resolvable magnitude
u-windspeed (m s^{-1})	0.06	0.6
v-windspeed (m s^{-1})	0.07	0.7
w-windspeed (m s^{-1})	0.06	0.6

The above results gave the nominal precision for wind measurement that does not consider the influence of environmental conditions. Changes in the environment will lead to sensor drift, increasingly deteriorating the measurement with flight duration (Metzger et al., 2012; Lenschow and Sun, 2007). Following the methods of Lenschow and Sun (2007), the ability of wind measurements from UAV to resolve the mesoscale variations of the 3D wind components in the encountered atmospheric conditions was assessed. For the vertical wind, the mesoscale variability was defined as the peak signal magnitude of the power spectra curve. The corresponding average wavenumber was determined as 0.09 m^{-1} based on the straight flight leg (about 4 km, lasting about 120 s) of the standard operational flight. Then, according to Eq. (1), the minimum required signal level for the vertical wind measurement was estimated as $\partial w/\partial t \simeq 0.14$ m s^{-2}. The accuracy of the vertical wind measurement using Eq. (2) is estimated as follows. The first term on the right-hand side of Eq. (2) is dominated by the drift in the differential pressure transducer, the value of $\partial U_a = 0.05$ m s^{-1} acquired from the wind tunnel test was used (Table 1). The histogram of Θ derived from the standard operational flights is shown in Figure 5. The 99 % confidence interval indicates that the value of Θ seldom exceeds $\pm 3°$, i.e., ± 0.053 radians. Thus, the value of the first term was estimated as 2.2×10^{-5} m s^{-2}.
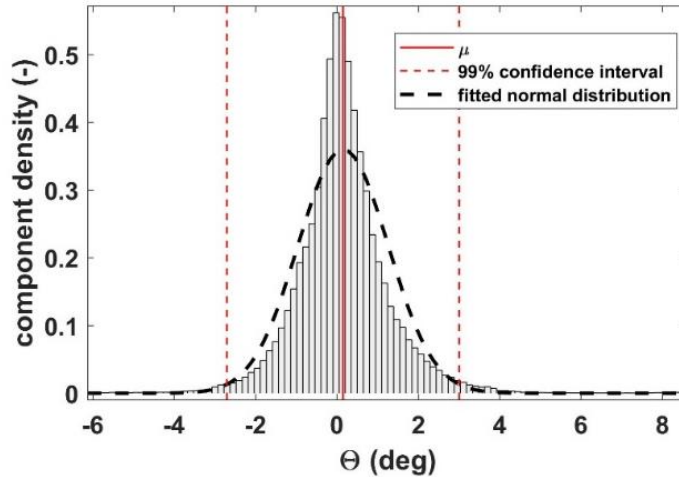
439

440 **Figure 5. Histogram of Θ derived from the standard operational flights. Component density is scaled so that the histogram has a**
441 **total area of one. Red vertical lines indicate distribution average (solid) and 99% confidence interval (dashed). The black dashed**
442 **bell curve displays a reference fitted normal distribution.**

443   The second term in Eq. (2) is a combination of INS pitch accuracy and 5HP attack angle accuracy. The combined accuracy

444 of these two sensors were applied to derive $\partial\Theta = 0.0024$ radians. Thus, the second term in Eq. (2) was estimated as

445 6×10^{-4} m s^{-2}. Finally, the third term in Eq. (2) was estimated as 1.7×10^{-4} m s^{-2}, according to the stated accuracy of the

446 vertical velocity from the INS. The overall performance of the vertical wind measurement (7.9×10^{-4} m s^{-2}) was accurate

447 enough to resolve the mesoscale variations in vertical air velocity.

448   The required accuracy of horizontal wind for mesoscale measurement was estimated as 10 times larger than that of vertical

449 wind, i.e., $\partial u/\partial t \simeq \partial v/\partial t \simeq 1.4$ m s^{-2}. The measurement accuracy of the horizontal wind component u was estimated as

450 4.8×10^{-4} m s^{-2} according to Eq. (3). Like the first term in Eq. (2), with the value of Ψ rarely exceeding ±0.18 radians, the

451 measurement accuracy of the horizontal wind component v was estimated as 2.7×10^{-2} m s^{-2}according to Eq. (4). Thus, the

452 measurement accuracy of the horizontal wind components was accurate enough to resolve the mesoscale variations in the

453 horizontal air velocity as well.

454   Second, before checking the quality of the acquired calibration parameters, the calibration results of the offset in pitch (ϵ_θ)

455 and heading (ϵ_ψ) angles based on the 'box' maneuver are provided in Supplement Part C (Figs. S2 and S3). The final calibration

456 values are $\epsilon_\theta = -0.183°$ and $\epsilon_\psi = 2°$. In order to verify the quality of these calibration parameters, a 'racetrack' maneuver

457 was performed. Figure 6 shows the validation results by plotting wind vector and calculating summary statistics for the

458 'racetrack' maneuver (including turns), using the initial ($\epsilon_\theta = \epsilon_\psi = 0°$, Fig. 6a) and calibrated (Fig. 6b) set of parameters,

459 respectively. Introduction of the calibration parameter effectively improved the quality of geo-referenced wind vector

460 measurement. The standard deviation for wind direction, $\sigma_{U_{dir}}$, is 4.9° for the calibrated set compared to 8.7° for the initial

461 set, and the standard deviation of wind speed, σ_U, is 0.52 m s^{-1} for the calibrated set compared to 1.12 m s^{-1} for the initial set.

462   The averaged vertical wind speed is much closer to zero ($\overline{w} = -0.006$ m s^{-1}) for the calibrated set than for the initial set ($\overline{w} =$

463   0.1 m s^{-1}). For the horizontal wind, it is evident from Fig. 6 that the measurement of wind direction and velocity are little

464   affected by sharp turns. On the contrary, the measurement of the vertical wind component is obviously affected by turns in

465   flight, as shown by the large fluctuations in the vertical wind speed around the scan value of 150 (bottom panels in Fig. 6). It

466   should be noted that the influence of upwash flow and the leverage effect are not considered in the calculated geo-referenced

467   wind vector.
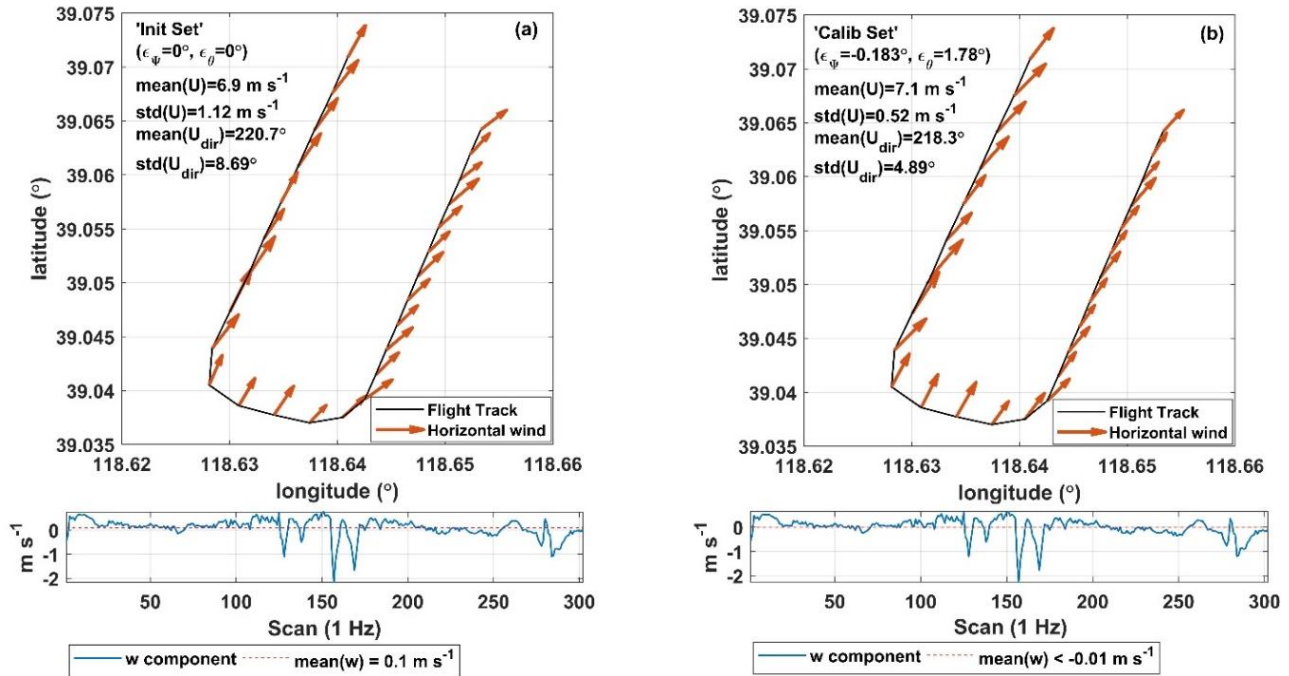
468

469 **Figure 6. Quality check of the calibration parameter by plotting wind vector and calculating summary statistics for the 'racetrack'**
470 **maneuver, using the initial (a) and calibrated (b) set of parameters, respectively. The calibration flight was carried out on 4**
471 **September 2022 at the Caofeidian Shoal Harbor in the Bohai Sea of northern China.**

472   Third, in order to check the influence of the lift-induced upwash on the measured attack angle from the 5HP, an 'acceleration-

473   deceleration' flight maneuver was performed. During the 'acceleration-deceleration' maneuver, INS data shown a vertical

474   velocity of the UAV at 0.05±0.2 m s^{-1}, the altitude of UAV at 392±0.6 m, the heading of UAV at 199±2.4° . We assumed that

475   the flight conditions meet the requirements of the 'acceleration-deceleration' maneuver (Vellinga et al., 2013). The relationship

476   between the pitch angle (θ) measured by the INS and the attack angle (α) measured by the 5HP is plotted in Figure 7, where

477   the attack angle was not corrected for lift-induced upwash. The slope (0.94) between θ and α is close to its theoretical value

478   of 1, and the intercept (0.16) is close to zero. It indicates that the lift-induced upwash has only a very small effect on the attack

479   angle, and the influence of upwash could be ignored.

480
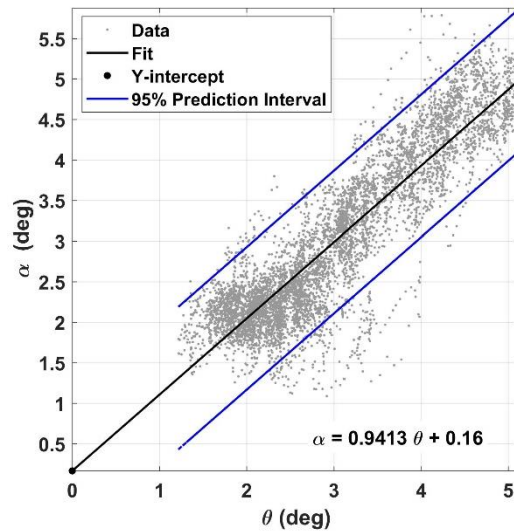
Figure 7. Relationship between the pitch angle (θ) measured by the integrated navigation system (INS) and the attack angle (α) measured by the 5-hole probe (5HP). The fitted linear equation is also shown.

483   Finally, the geo-referenced wind vector was calculated with and without the correction for the leverage effect based on the

484   measurement data from the 'acceleration-deceleration' flight maneuver. The averaged relative differences between the

485   corrected and uncorrected horizontal and vertical wind speeds are 0.1 % and 0.2 %, respectively. The standard deviation for

486   horizontal wind speed is 0.307 m s^{-1} without the level arm term compared to 0.306 m s^{-1} when the level arm term is introduced.

487   The standard deviation of vertical wind speed is 0.254 m s^{-1} without the level arm term compared to 0.253 m s^{-1} with the level

488   arm term. The correction of leverage effect had minimal effect on improving the geo-referenced wind vector measurement;

489   therefore, this correction term can be ignored.

490   **3.2 Flux measurement error caused by instrumental noise**

491   Flux measurement error caused by the instrumental noise gives the lowest limit of the value that the UAV-based EC system is

492   able to measure. It was assessed by combining the covariance uncertainty estimated by RS method and the propagation of

493   errors in flux correction terms. Before estimating the flux covariance uncertainty using RS method, using the measured data

494   from each straight and level flight leg of the standard operational flight (Fig. 2), the normalized integrated cospectra (ogives)

495   curves of sensible heat (Fig. 8a), latent heat (Fig. 8b), and CO_2 (Fig. 8c) flux are formed as a function of wavenumber (k),

496   where $k = 2\pi f / U_a$. As shown in Figure 8, although the heterogeneous turbulence (or mesoscale turbulence) interfered the

497   shape of ogive curves, most curves converged at the high and low frequency ends, which indicated that these segmented data

498   were sufficiently long to represent the lowest significant frequencies contributing to the covariance (Sun et al., 2018).

499
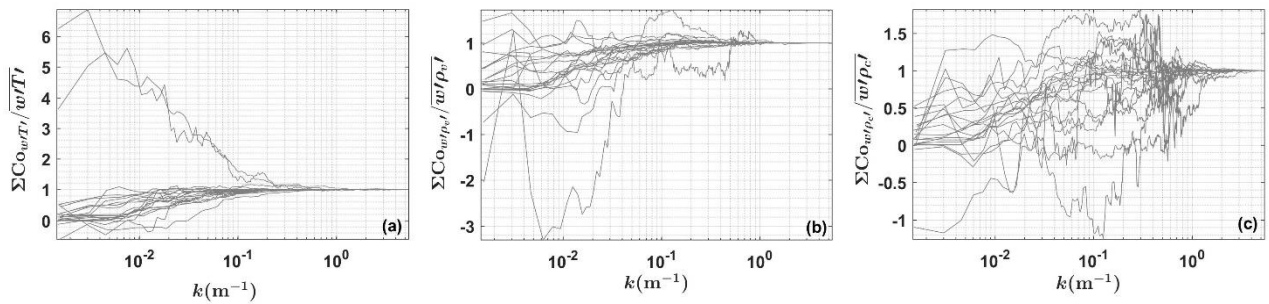
Figure 8. Normalized ogive curves as a function of wavenumber for the flux covariance of sensible heat (a), latent heat (b), and CO_2 (c) from each straight and level flight leg of the standard operational flights in Section 2.2.2.

The results of instrumental noise related relative flux measurement error compared to the magnitude of the flux are shown in Figure 9. It can be seen that the flux measurement error caused by instrumental noise significantly decreases when the flux magnitude increases. It is not surprising since, in theory, instrumental noise is usually close to a constant and the relative flux measurement error caused by instrumental noise will decreases with increasing measurement magnitude. Overall, instrumental noise has the least effect on latent heat flux (ranging from 0.02% to 2.42% in this study) measurements, followed by sensible heat flux (ranging from 0.05% to 8.6% in this study), and has the greatest effect on the measurement of CO_2 flux (ranging from 0.22% to 75.6% in this study). Then, a simple rational function relationship between the relative measurement error and the flux magnitude is fitted according to the measured data, where the constant term in the denominator is set to 0. The fitted coefficient in the numerator can be considered as the flux measurement error caused by instrumental noises, which are 0.03 µmol m^{-2} s^{-1}, 0.02 W m^{-2}, and 0.08 W m^{-2} for the measurement of CO_2 flux, sensible and latent heat flux, respectively. At last, using the signal-to-noise ratio of 10:1, the minimum magnitudes for reliably resolving the CO_2 flux, sensible and latent heat fluxes were estimated as 0.3 µmol m^{-2} s^{-1}, 0.2 W m^{-2}, and 0.8 W m^{-2}, respectively.

514
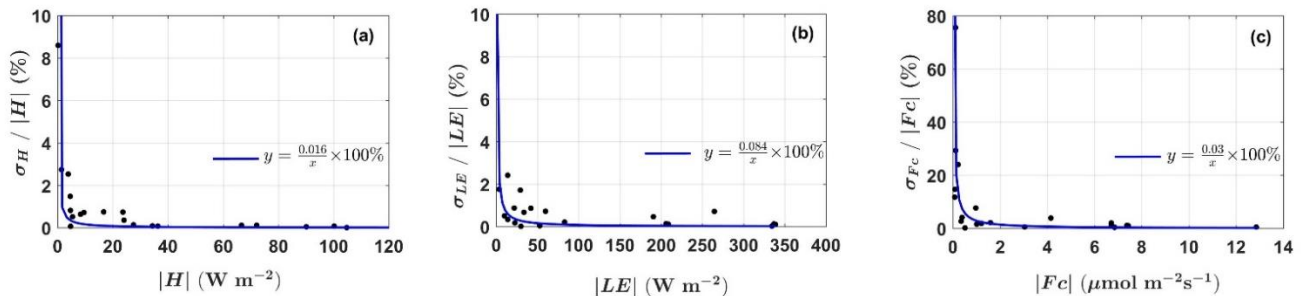
Figure 9. Relative flux measurement error caused by the instrumental noise plotted against the magnitude of the flux. Also shown the fitted error curves. Measured data was from the standard operation flights in Section 2.2.2.

3.3 Resonance noise

The resonance noise from the engine and propeller can lead to systematic overestimation of the variance and covariance of the observed atmospheric scalars. The noise mainly appears in the high frequency domain of the (co)spectra, and the reference (co)spectral curve of Massman and Clement (2005) was used to quantify the systematically bias caused by the resonance noise.

521   All spectra curves of the variance of the measured scalars (including air temperature, H_2O, and CO_2 concentration)

522   approximately followed the reference spectra curve and the reference -2/3 slope in the inertial subrange (Figs. 3a to 3c). The

523   largest scatter occurred in the spectra of CO_2 (Fig. 3c). When comparing the spectra curve with the reference spectra, the

524   resonance noise led to a systematic deviation in the variance of air temperature, H_2O, and CO_2 concentration of 0.1 ± 0.1 %,

525   1.0 ± 0.79 %, and 4.4 ± 0.66 %, respectively. For the flux covariance of sensible, latent heat and CO_2, all the co-spectra curves

526   approximately follow the reference co-spectra curve and the reference -4/3 slope in the inertial subrange (Figs. 3d to 3f).

527   Compared with the reference co-spectra, the resonance noise led to a systematic deviation in the flux of sensible, latent heat,

528   and CO_2 of 0.07 ± 0.004 %, 0.3 ± 0.25 %, and 2.9 ± 1.62 %, respectively.

529   The results show that the resonance noise has a very little impact on the measured variance and flux covariance. The

530   measurements of CO_2 concentration and flux are most susceptible to the resonance noise, but the impact of this noise is limited

531   to around 5 % of the observed value.

532   **3.4 Sensitivity analysis**

533   In order to investigate the relevance of the calibration parameters for the measurement of the geo-referenced wind vector and

534   turbulent flux, two sensitivity tests were conducted by adding an error of ±30 % to the used calibrated parameters

535   $(\epsilon_\psi, \epsilon_\theta, \epsilon_\phi, \epsilon_r)$. We assumed that the maximum uncertainties contained in the calibration parameter is not more than 30 % of

536   its own value.

537   First, the sensitivity of the geo-referenced 3D wind and turbulent flux to the uncertainty in the individual calibration

538   parameter was tested. The RE value is used to quantify the sensitivity, and the results are summarized in Tables 3 and 4. For

539   the measurement of the geo-referenced wind vector, Table 3 shows that the uncertainties in the temperature recovery factor

540   (ε_r) and 5HP mounting misalignment error in the roll (ϵ_ϕ) angle do not contribute significantly to errors in the wind

541   measurements, which were typically smaller than 4% of the observed value in this study. Parameter ε_θ had the largest effect

542   on the vertical wind component (up to 30 %), whereas ε_ψ had the largest effect on the horizontal wind component. For the

543   measurement of turbulent fluxes, Table 4 shows that the errors in ε_r and ϵ_ϕ does not significantly influence the flux

544   measurements, typically small than 5% of the observed value in this study. Uncertainties in calibration parameter ε_θ and ε_ψ

545   had significant effects on the measurement of turbulent fluxes. Errors in ε_θ result in significant perturbation (large RE variance)

546   in the measured turbulent fluxes including sensible heat, latent heat and CO_2. While, errors in ε_ψ to some extent mainly affect

547   the measurement of latent heat flux (RE may up to 15 %).

548   **Table 3**: RE from the sensitivity test for the geo-referenced 3D wind vector (u, v, w). An error factor of ±30 % was added to

549   each calibrated parameter. The geo-referenced 3D wind vector was calculated based on the straight leg of the standard

550   operational flight.

Parameter	Error (%)	RE of geo-referenced 3D wind vector mean ± std

		u (%)	v (%)	w (%)
ε_r	-30	0.04±0.41	-0.004±2	0±0
	30	0.06±0.43	0.27±1.1	-0.07±0.23
ε_φ *	-30	0.41±2.51	-0.09±2.05	1.15±2.43
	30	-0.43±2.61	0.09±1.79	-1.1±2.66
ε_θ	-30	0.03±0.41	-0.35±2.54	-30.51±6.42
	30	0.05±0.45	0.42±1.82	30.37±6.61
ε_ψ	-30	2.98±25.06	-2.04±16.3	0±0
	30	-2.97±24.96	2.42±16.63	0±0

551   * The optimum calibration value is set to 0, ε_φ was varied over ±0.9°, which is 30 % of its typical range.

552   **Table 4**: *RE* from the sensitivity test for the turbulent fluxes. An error factor of ±30 % was added to each calibrated parameter.

553   The turbulent fluxes were calculated based on the straight leg of the standard operational flight.

Parameter	Error (%)	*RE* of turbulent flux mean ± std			
		Fc (%)	*H* (%)	LE (%)	u* (%)
ε_r	-30	1.04±3.04	-0.76±4.82	0.1±0.29	0±0
	30	-1.0±3.3	0.74±4.8	-0.1±0.29	0.2±1.07
ε_φ *	-30	0.07±1.2	0.03±0.7	0.15±1.51	0.54±1.71
	30	-0.14±0.89	-0.06±0.7	-0.16±1.46	0.12±1.61
ε_θ	-30	-3.27±11.18	-0.8±9.48	0.19±11.91	-4.08±5.61
	30	2.34±10.52	-0.44±8.24	-1.27±9.92	3.73±4.53
ε_ψ	-30	1.78±5.18	-0.73±4.87	1.89±13.42	0.63±5.75
	30	-0.99±3.96	-0.57±3.26	2.66±11.76	-0.59±4.42

554   * See Table 3.

555   The second sensitivity test was performed to evaluate the overall interaction between calibration parameters and the

556   calculation of geo-referenced wind vector and turbulent flux by adding an error of ±30 % to all the calibration members

557   simultaneously. Tables 5 and 6 provided a summary of the *RE* from the second sensitivity test. For the measurement of geo-

558   referenced wind vector (Table 5), adding an error of ±30 % to all the calibration parameters at the same time resulted in great

559   perturbations to both the horizontal (low *RE* with high variance) and vertical wind components (high *RE* with low variance).

560   For the measurement of turbulent fluxes, adding 30% error in all of the calibration parameters can result in errors in the

561   measured fluxes more than 10%. In addition, Table 6 also reveals that the latent heat flux is more sensitivity to the errors in

562   the calibration parameter than other measured fluxes (higher mean and variance of the *RE* compared to other measurements).

563   **Table 5**: *RE* from the sensitivity test for the geo-referenced 3D wind vector (u, v, w) calculated by adding an error of ±30 %

564   to all the calibrated parameter simultaneously. The geo-referenced 3D wind vector was calculated based on the straight leg of

565   the standard operational flight.

Parameter	Error (%)	*RE* of geo-referenced 3D wind vector mean ± std		
		u (%)	v (%)	w (%)

| | -30 | 4.24±27.89 | -3.2±21.1 | -29.35±4.63 |
| All | 30 | -4.15±27.46 | 3.55±21.91 | 29.16±4.86 |

Table 6: *RE* from the sensitivity test for the turbulent flux calculated by adding an error of $\pm 30\%$ to all the calibrated parameter simultaneously. The turbulent flux was calculated based on the straight flight leg of the standard operational flight.

Parameter	Error (%)	*RE* of turbulent flux mean ± std			
		Fc (%)	*H* (%)	LE (%)	u* (%)
All	-30	-1.19±10.51	-0.9±8.06	2.71±13.91	-2.92±8.19
	30	-0.49±10.01	-1.66±5.4	-6.07±13.24	1.74±6.55

4 Discussions

The current study aimed to evaluate the performance of the UAV-based EC system developed by Sun et al. (2021a) in the measurement of wind vector and turbulent flux.

First, the wind measurement precision (nominal precision) of the UAV-based EC system was estimated by propagating the sensor errors to the geo-referenced wind vector using the linearized Taylor series expansions from Enriquez and Friehe (1995) . The 1σ precision for geo-referenced wind measurement was estimated to be ± 0.07 m s^{-1}, and the least resolvable magnitude for wind measurement was estimated at 0.7 m s^{-1} by assuming the minimum signal-to-noise ratio of 10:1. The derived wind measurement minimum resolvable magnitude can be used as a basic reference for wind measurement capability of the UAV-based EC system, and the measured values of wind vector smaller than the minimum resolvable values should be considered unreliable. The accuracy of the sensors was also assessed by examining the collected data in the real environment. Our results revealed that the overall performance of geo-referenced wind measurement is sufficient accuracy for resolving the mesoscale variations of the 3D wind components under the encountered atmospheric conditions. Therefore, it is possible to capture the mesoscale variability of the atmospheric boundary layer (ABL) over a wide range of spatial scales by performing long flight paths.

Second, based on the measurement data from the in-flight calibration campaign, several key factors affecting the accuracy of geo-referenced wind measurement were analysed. The UAV-based EC system was calibrated (in Supplement Part C) using measured data from the 'box' flight maneuver to correct the mounting misalignment between the 5HP and the CG of the UAV in the heading ($\epsilon_\theta = -0.183°$) and pitch ($\epsilon_\psi = 2°$) angles. The quality of the acquired calibration parameters was verified using the measured data from 'racetrack' flight maneuver, and the acquired calibration value effectively improved the observed wind field with smaller variance compared with the wind calculated using their initial value. At the same time, the measurement of the vertical wind component was significantly affected by the in-flight turn (maintaining about 20° roll). Therefore, it is necessary to avoid using the measured data from the turn section for turbulent flux calculation. Compared to other studies (Vellinga et al., 2013; Reineman et al., 2013), the relatively large variance in the horizontal wind and wind direction after

591 calibrated in this study may be caused by the nonstationary condition of the turbulence. This was caused by the reason that the

592 flight altitude of 400 m was not high enough to totally avoid interaction from the underlying surface.

593   The current calibration procedure did not include methods to determine the offset angle in roll (ε_φ) and the temperature

594 recovery factor (ε_r) because of the small vertical separation (27.3 cm) between the 5HP and the roll axis of the UAV and the

595 small Mach number (<0.1) during operational flight. The default ($\varepsilon_\varphi = 0°$) and empirical ($\varepsilon_r = 0.82$) value were adopted for

596 these two calibration parameters. The sensitivity analysis shown these two parameters have no large effect on the wind vector

597 and turbulent flux.

598   It should be noted that wind measurement from the airborne platform may be susceptible to flow distortion and rigid-body

599 rotation (leverage effects). Generally, the influence of these two factors were ignored by UAV platform. To confirm that these

600 effects could be safely ignored, data from 'acceleration-deceleration' flight maneuver was used to analyse the effects of lift-

601 induced upwash and the leverage effect on the wind measurements. Our results demonstrated that the upwash has almost no

602 effect on the wind measurement, which was indicated by the near 1:1 relationship (0.94 in Fig. 7) between the measured attack

603 angles and pitch angle. The slight departures from the ideal 1:1 relationship may have been caused by the nonstationary

604 condition during the flight. For the influence of the leverage effects, the differences in 3D wind vector between corrected and

605 uncorrected for the leverage effect is very small as well. Ignoring the influence of the leverage effect has almost no effect on

606 the measurement of wind. Therefore, we concluded that the geo-referenced 3D wind vector can be measured reliably by the

607 current UAV-based EC system without considering the interference from the lift-induced upwash and leverage effects.

608   Third, instrumental noise related flux measurement error was estimated by combining the covariance uncertainty estimated

609 by RS method and the propagation of errors in flux correction terms. By assuming that the instrumental noise was close to a

610 constant, we fitted a simple rational function relationship between the relative measurement error and the flux magnitude

611 according to measured data (Fig. 9), and the fitted coefficient in the numerator can be considered as the flux measurement

612 error caused by instrumental noises. The estimated instrumental noise related flux measurement error of CO_2, sensible and

613 latent heat flux were 0.03 $\mu mol\ m^{-2}\ s^{-1}$, 0.02 $W\ m^{-2}$, and 0.08 $W\ m^{-2}$, respectively. Since the RS method directly uses the

614 shuffled raw measurement data to calculate the instrumental noise in the flux covariance, its estimates inevitably included the

615 effects of resonance noise from the UAV. Using the signal-to-noise ratio of 10:1, the least resolvable magnitude for turbulent

616 flux measurement was estimated to be 0.3 $\mu mol\ m^{-2}\ s^{-1}$ for the CO_2 flux, 0.2 $W\ m^{-2}$ for the sensible heat flux, 0.8 $W\ m^{-2}$ for

617 the latent heat flux, respectively.

618   Fourth, because that the UAV-based EC system has not completely insulated the noise from the operation of the engine and

619 propeller and its effect on the measured scalars, the reference (co)spectra of Massman and Clement (2005) was used to quantify

620 the effect of the resonance noise on the variance and flux covariance of the measured scalars. Due to the influence of resonance

621 noise mainly appeared in the high frequency domain, we artificially designated the frequency range of noise region for air

622 temperature, water vapor and CO_2 (Section 2.4.3). By calculating the area difference between the measured and reference

623 (co)spectral curves for the designated frequency range, the resonance effect could be quantified. The results shown that, overall,

624 resonance noise has little impact on the variance and flux covariance of the measured scalars. The measurements of CO_2

625 concentration and its flux covariance were the most susceptible to resonance noise, but the maximum effect was less than 5 %.

626 It should be noted that this method may overestimate the deviation caused by the resonance noise due to the reference

627 (co)spectra curve and the measured (co)spectra not fully overlapping in the inertial subrange (shown in Fig. 3).

628   Fifth, two sensitivity tests were conducted to assess the perturbation of the geo-referenced wind velocity and turbulent flux

629 under variation (±30 %) of each calibration parameter around its calibrated value ($\epsilon_\psi = 2°, \epsilon_\theta = -0.183°, \epsilon_\phi = 0°, \epsilon_r =$

630 0.82) as well as under simultaneous variation (±30 %) of all calibration parameters. Their RE was used to evaluate the

631 sensitivity, and values of wind and flux less than their least resolvable magnitude were removed from this analysis. The results

632 revealed that uncertainties in the temperature recovery factor (ε_r) and mounting offset in roll angle (ε_φ) do not significantly

633 contribute to an error in the measurement of wind vector ($RE < 4\%$) and turbulent fluxes ($RE < 5\%$). Calibration parameters

634 that had the largest effect on the measurement of geo-referenced wind vector and turbulent flux are the mounting offset angle

635 in pitch (ε_θ) and heading (ε_ψ). Uncertainties in ε_θ had a direct effect on the measurement of vertical wind component, and

636 then these errors propagate to the measured fluxes, resulting in a large error contained in the measured fluxes (~15 %). A

637 negative error in ε_θ will lead to an underestimation of the vertical wind and vice versa. Errors in ε_ψ directly affect the

638 measurement of the horizontal wind, and to some extent, the measurement of turbulent flux. By checking the relationship

639 between the magnitude of the horizontal wind (u, v) and RE, a near rational function relationship was seen, as shown in Figure

640 10. The influence of the error in the ε_ψ decreased significantly with the increase in the magnitude of the horizontal wind

641 velocity. Additionally, the measurement of latent heat flux may be greatly affected by the error in ε_ψ, which is reflected by the

642 relatively large deviancy (~14 %) of the RE. Therefore, the parameter ε_θ and ε_ψ need to be carefully calibrated.
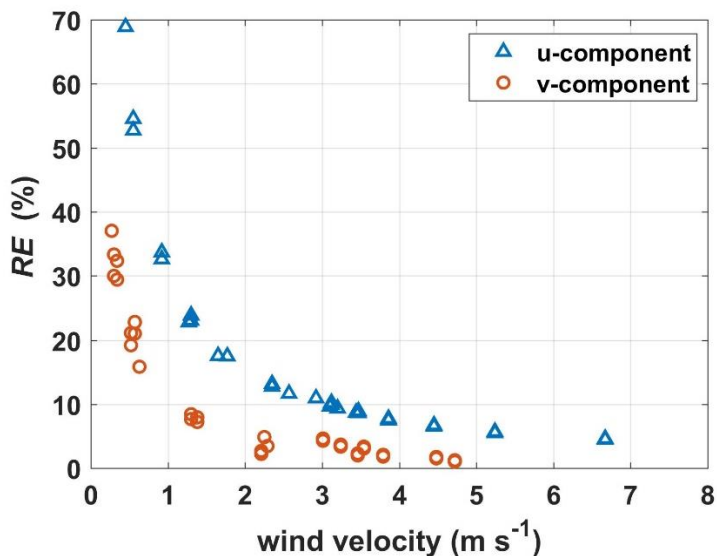
643

644 **Figure 10. Relationship between the magnitude of the horizontal wind velocity (u, v) and the relative error (RE) from the sensitivity**
645 **test.**

646 Lastly, it should be noted that the accuracy of the measured geo-referenced wind field and turbulent flux from the UAV-

647 based EC system is subject to the combination of many factors, mainly including sensor accuracy, UAV powerplant, UAV

648 fluctuation (e.g., variation of the UAV attitude and flight height), and the atmospheric conditions during the measurements,

649 etc. This study mainly focused on assessing the effects of sensor precision and UAV powerplant on the measurement errors of

650 geo-referenced wind vector and turbulent flux. Evaluation results gave the lowest limit of the wind field and turbulent flux that

651 the UAV-based EC system can measure reliably. Direct comparison of flux measurements between aircraft and traditional

652 ground tower is still challenging due to the difference in the measurement height, mechanism (time series for ground EC and

653 space series for aircraft), and instruments (e.g., wind sensor). Previous studies have extensively compared the measurement of

654 fluxes and wind vector between airborne and ground-based EC methods and found consistent results (Gioli et al., 2004;

655 Metzger et al., 2012; Sun et al., 2021b). At the same time, substantial and consistent over- or under- estimation of the measured

656 wind and fluxes by aircraft compared to ground measurements were observed and reported. These differences may be due to

657 several factors such as vertical flux divergence (the measurement height of UAV is higher than ground-tower), surface

658 heterogeneity (induced by the larger footprint region of the UAV compared to the ground tower), measurement errors (e.g.,

659 window length, resonance noise, etc.) as well as their difference in platform and sensors. Therefore, in order to evaluate the

660 measurement performance of the UAV-based EC system realistically, it is necessary to conduct a comparison test on the same

661 platform and under the same environment to exclude the influence of these factors.

662 **5 Conclusions and further works**

663 The main objective of this study was to quantitatively evaluate the performance of the developed UAV-based EC system in

664 the measurement of geo-referenced wind field and turbulent flux. In terms of measuring precision, magnitudes larger than 0.7

665 m s^{-1} for wind velocity, 0.3 µmol m^{-2} s^{-1} for CO_2 flux, 0.2 W m^{-2} for sensible heat flux, and 0.8 W m^{-2} for latent heat flux could

666 be reliably measured by the UAV-based EC system. Carefully calibrated offset angle in pitch (ϵ_θ) and heading (ϵ_ψ) were

667 shown to effectively improve the quality of wind field measurements, and the influences of flow distortion and the leverage

668 effect on the wind measurement were minimal and could be ignored. The influence of resonance noise was small on the

669 measurement of air temperature and water vapor (typically < 1 % for their variance and flux covariance), but relatively large

670 on the measurement of CO_2 (around 5 % for variance and flux covariance).

671 The relevance of the calibration parameters ($\varepsilon_r, \epsilon_\phi, \varepsilon_\psi, \varepsilon_\theta$) for the measurement of the geo-referenced wind vector and

672 turbulent flux was also assessed based on two sensitivity tests. The measurements of the geo-referenced wind vector and

673 turbulent flux were insensitive to the errors in the ε_r and ϵ_ϕ. While uncertainties in the calibration parameters ε_θ and ε_ψ had

674 the strongest effects on the measurements. Because of ε_θ determining the magnitude of the vertical wind, its error will directly

675 lead to uncertainties in vertical wind measurement and then propagate the uncertainties to the measured turbulent flux. Errors

676 in ε_ψ have a direct effect on the measurement of horizontal wind, and to some extent, the measurement of turbulent flux.

677 Therefore, these two calibration parameters need to be carefully calibrated. Conducting the UAV-based EC measurement when

678 wind velocity is larger than 3 m s^{-1} can led to more stable and reliable ($RE < 10\%$) results of the wind speed measurement

679 compared to a relatively windless environmental.

680   Finally, we concluded that the developed UAV-based EC system measured the geo-referenced wind field and turbulent flux

681 with sufficient precision. The lift-induced upwash and leverage effect had almost no effect on the measurement of geo-

682 referenced wind vector. The resonance effect caused by the operation of engine and propeller mainly affected the measurement

683 of CO_2, and its effect on variance and flux covariance was around 5 %. The quality of calibration parameters ε_ψ and ε_θ has a

684 significant effect on the measurements of the geo-referenced wind vector and turbulent flux, which underscores the importance

685 of careful calibration. The UAV-based EC system has several advantages over manned aircraft, including less turbulence

686 disturbance in wind measurement, lower measurement altitude (above the ground level), simpler operation, and lower

687 operating costs, etc. However, there are still some shortcomings need to be overcome, such as resonance noise, how large the

688 difference compared to the tower-based EC under the same conditions, and how to interpret the instantaneous flux results for

689 the flight scenario (e.g., influence from surface heterogeneity, flux divergence, etc.). Future researches may include the

690 development of a new UAV-based EC system with the following improvements: 1) a new electro-powered UAV platform

691 with the advantages of being quieter (low noise), having a low cruising speed; 2) a ground-vehicle-based validation platform

692 to enable direct comparative evaluation of the UAV-based EC system with traditional ground EC methods under near-identical

693 environmental conditions; 3) a graphics based real-time monitoring system to make it possible to change the flight pattern

694 according to real-time data; and 4) conducting a number of integrated field observation experiments that combining tower-

695 based EC networks, OMS, and multi-source satellite RS to further prompt the development of theory and methodology for

696 airborne flux measurements. Ultimately, the versatility of the UAV-based EC system as a low cost and widely applicable

697 environmental research aircraft will further improve our understanding of the energy and matter cycling processes at the

698 regional scales.

699 ***Author contributions.*** SY, GB and LX planned the field campaign; SY, LB, JJ, ZZ and JS carried out the field measurements.

700 SY, LS and XZ analysed the data and wrote the manuscript draft. SB, and QZ reviewed and edited the manuscript.

701 ***Competing interests.*** The authors declare that they have no conflict of interest.

702 ***Acknowledgments.*** This work was supported jointly by the Fundamental Research Funds for the Central Public-interest

703 Scientific Institution (Grant No. 2023YSKY-27), and the National Natural Science Foundation of China (Grant No. 42101477).

704 We would like to thank F-EYE UAV Technology Co. Ltd. for building, maintaining, and operating the UAV in this study.

705 We would like to thank Dr. Joseph Elliot at the University of Kansas for her assistance with English language and grammatic

706 al editing of the manuscript.

707 ***Data availability.*** Data for this research are not publicly available due to its proprietary nature currently. The UAV calibration

708 flight data and the standard operation flight data in this study are available upon request to the corresponding author.

References

Anderson, K. and Gaston, K. J.: Lightweight unmanned aerial vehicles will revolutionize spatial ecology, Frontiers in Ecology and the Environment, 11, 138-146, https://doi.org/10.1890/120150, 2013.

Båserud, L., Reuder, J., Jonassen, M. O., Kral, S. T., Paskyabi, M. B., and Lothon, M.: Proof of concept for turbulence measurements with the RPAS SUMO during the BLLAST campaign, Atmos. Meas. Tech., 9, 4901-4913, 10.5194/amt-9-4901-2016, 2016.

Billesbach, D. P.: Estimating uncertainties in individual eddy covariance flux measurements: A comparison of methods and a proposed new method, Agricultural and Forest Meteorology, 151, 394-405, https://doi.org/10.1016/j.agrformet.2010.12.001, 2011.

Calmer, R., Roberts, G. C., Sanchez, K. J., Sciare, J., Sellegri, K., Picard, D., Vrekoussis, M., and Pikridas, M.: Aerosol–cloud closure study on cloud optical properties using remotely piloted aircraft measurements during a BACCHUS field campaign in Cyprus, Atmos. Chem. Phys., 19, 13989-14007, 10.5194/acp-19-13989-2019, 2019.

Chandra, N., Patra, P. K., Niwa, Y., Ito, A., Iida, Y., Goto, D., Morimoto, S., Kondo, M., Takigawa, M., Hajima, T., and Watanabe, M.: Estimated regional CO_2 flux and uncertainty based on an ensemble of atmospheric CO_2 inversions, Atmos. Chem. Phys., 22, 9215-9243, 10.5194/acp-22-9215-2022, 2022.

Chen, J. M., Leblanc, S. G., Cihlar, J., Desjardins, R. L., and MacPherson, J. I.: Extending aircraft- and tower-based CO_2 flux measurements to a boreal region using a Landsat thematic mapper land cover map, Journal of Geophysical Research: Atmospheres, 104, 16859-16877, https://doi.org/10.1029/1999JD900129, 1999.

Chen, W., Wang, D., Huang, Y., Chen, L., Zhang, L., Wei, X., Sang, M., Wang, F., Liu, J., and Hu, B.: Monitoring and analysis of coastal reclamation from 1995–2015 in Tianjin Binhai New Area, China, Scientific Reports, 7, 3850, 10.1038/s41598-017-04155-0, 2017.

Chu, H., Luo, X., Ouyang, Z., Chan, W. S., Dengel, S., Biraud, S. C., Torn, M. S., Metzger, S., Kumar, J., Arain, M. A., Arkebauer, T. J., Baldocchi, D., Bernacchi, C., Billesbach, D., Black, T. A., Blanken, P. D., Bohrer, G., Bracho, R., Brown, S., Brunsell, N. A., Chen, J., Chen, X., Clark, K., Desai, A. R., Duman, T., Durden, D., Fares, S., Forbrich, I., Gamon, J. A., Gough, C. M., Griffis, T., Helbig, M., Hollinger, D., Humphreys, E., Ikawa, H., Iwata, H., Ju, Y., Knowles, J. F., Knox, S. H., Kobayashi, H., Kolb, T., Law, B., Lee, X., Litvak, M., Liu, H., Munger, J. W., Noormets, A., Novick, K., Oberbauer, S. F., Oechel, W., Oikawa, P., Papuga, S. A., Pendall, E., Prajapati, P., Prueger, J., Quinton, W. L., Richardson, A. D., Russell, E. S., Scott, R. L., Starr, G., Staebler, R., Stoy, P. C., Stuart-Haëntjens, E., Sonnentag, O., Sullivan, R. C., Suyker, A., Ueyama, M., Vargas, R., Wood, J. D., and Zona, D.: Representativeness of Eddy-Covariance flux footprints for areas surrounding AmeriFlux sites, Agricultural and Forest Meteorology, 301-302, 108350, https://doi.org/10.1016/j.agrformet.2021.108350, 2021.

Crawford, T. L. and Dobosy, R. J.: A sensitive fast-response probe to measure turbulence and heat flux from any airplane, Boundary-Layer Meteorology, 59, 257-278, 10.1007/BF00119816, 1992.

Crawford, T. L., Dobosy, R. J., and Dumas, E. J.: Aircraft wind measurement considering lift-induced upwash, Boundary-Layer Meteorology, 80, 79-94, 10.1007/BF00119012, 1996.

Desjardins, R. L., Brach, E. J., Alvo, P., and Schuepp, P. H.: Aircraft Monitoring of Surface Carbon Dioxide Exchange, Science, 216, 733-735, 10.1126/science.216.4547.733, 1982.

Desjardins, R. L., Worth, D. E., MacPherson, J. I., Bastian, M., and Srinivasan, R.: Flux measurements by the NRC Twin Otter atmospheric research aircraft: 1987–2011, Adv. Sci. Res., 13, 43-49, 10.5194/asr-13-43-2016, 2016.

Drüe, C. and Heinemann, G.: A Review and Practical Guide to In-Flight Calibration for Aircraft Turbulence Sensors, Journal of Atmospheric and Oceanic Technology, 30, 2820-2837, 10.1175/JTECH-D-12-00103.1, 2013.

Elston, J., Argrow, B., Stachura, M., Weibel, D., Lawrence, D., and Pope, D.: Overview of Small Fixed-Wing Unmanned Aircraft for Meteorological Sampling, Journal of Atmospheric and Oceanic Technology, 32, 97-115, 10.1175/JTECH-D-13-00236.1, 2015.

Enriquez, A. G. and Friehe, C. A.: Effects of Wind Stress and Wind Stress Curl Variability on Coastal Upwelling, Journal of Physical Oceanography, 25, 1651-1671, https://doi.org/10.1175/1520-0485(1995)025<1651:EOWSAW>2.0.CO;2, 1995.

Finkelstein, P. L. and Sims, P. F.: Sampling error in eddy correlation flux measurements, Journal of Geophysical Research: Atmospheres, 106, 3503-3509, https://doi.org/10.1029/2000JD900731, 2001.

Garman, K. E., Wyss, P., Carlsen, M., Zimmerman, J. R., Stirm, B. H., Carney, T. Q., Santini, R., and Shepson, P. B.: The Contribution of Variability of Lift-induced Upwash to the Uncertainty in Vertical Winds Determined from an Aircraft Platform, Boundary-Layer Meteorology, 126, 461-476, 10.1007/s10546-007-9237-y, 2008.

Garman, K. E., Hill, K. A., Wyss, P., Carlsen, M., Zimmerman, J. R., Stirm, B. H., Carney, T. Q., Santini, R., and Shepson, P. B.: An Airborne and Wind Tunnel Evaluation of a Wind Turbulence Measurement System for Aircraft-Based Flux Measurements, Journal of Atmospheric and Oceanic Technology, 23, 1696-1708, 10.1175/JTECH1940.1, 2006.

Gioli, B., Miglietta, F., Vaccari, F. P., and Zaldei, A.: The Sky Arrow ERA, an innovative airborne platform to monitor mass, momentum and energy exchange of ecosystems, Annals of Geophysics, 49, 109-116, 10.4401/ag-3159, 2006.

Gioli, B., Miglietta, F., De Martino, B., Hutjes, R. W. A., Dolman, H. A. J., Lindroth, A., Schumacher, M., Sanz, M. J., Manca, G., Peressotti, A., and Dumas, E. J.: Comparison between tower and aircraft-based eddy covariance fluxes in five European regions, Agricultural and Forest Meteorology, 127, 1-16, https://doi.org/10.1016/j.agrformet.2004.08.004, 2004.

Hannun, R. A., Wolfe, G. M., Kawa, S. R., Hanisco, T. F., Newman, P. A., Alfieri, J. G., Barrick, J., Clark, K. L., DiGangi, J. P., Diskin, G. S., King, J., Kustas, W. P., Mitra, B., Noormets, A., Nowak, J. B., Thornhill, K. L., and Vargas, R.: Spatial heterogeneity in CO2, CH4, and energy fluxes: insights from airborne eddy covariance measurements over the Mid-Atlantic region, Environmental Research Letters, 15, 035008, 10.1088/1748-9326/ab7391, 2020.

Hu, G. and Jia, L.: Monitoring of Evapotranspiration in a Semi-Arid Inland River Basin by Combining Microwave and Optical Remote Sensing Observations, Remote Sensing, 7, 10.3390/rs70303056, 2015.

Kaimal, J. C., Clifford, S. F., and Lataitis, R. J.: Effect of finite sampling on atmospheric spectra, Boundary-Layer Meteorology, 47, 337-347, 10.1007/BF00122338, 1989.

776   Kalogiros, J. A. and Wang, Q.: Aerodynamic Effects on Wind Turbulence Measurements with Research Aircraft, Journal of

777   Atmospheric and Oceanic Technology, 19, 1567-1576, 10.1175/1520-0426(2002)019<1567:AEOWTM>2.0.CO;2, 2002.

778   Khelif, D., Burns, S. P., and Friehe, C. A.: Improved Wind Measurements on Research Aircraft, Journal of Atmospheric and

779   Oceanic Technology, 16, 860-875, 10.1175/1520-0426(1999)016<0860:IWMORA>2.0.CO;2, 1999.

780   Kowalski, A. S., Serrano-Ortiz, P., Miranda-García, G., and Fratini, G.: Disentangling Turbulent Gas Diffusion from Non-

781   diffusive Transport in the Boundary Layer, Boundary-Layer Meteorology, 179, 347-367, 10.1007/s10546-021-00605-5, 2021.

782   Lenschow, D. H.: Aircraft Measurements in the Boundary Layer, in: Probing the Atmospheric Boundary Layer, edited by:

783   Lenschow, D. H., American Meteorological Society, Boston, MA, Boston, https://doi.org/10.1007/978-1-944970-14-7_5,

784   1986.

785   Lenschow, D. H. and Sun, J.: The spectral composition of fluxes and variances over land and sea out to the mesoscale,

786   Boundary-Layer Meteorology, 125, 63-84, 10.1007/s10546-007-9191-8, 2007.

787   Lenschow, D. H., Delany, A. C., Stankov, B. B., and Stedman, D. H.: Airborne measurements of the vertical flux of ozone in

788   the boundary layer, Boundary-Layer Meteorology, 19, 249-265, 10.1007/BF00117223, 1980.

789   Li, X., Liu, S., Xiao, Q., Ma, M., Jin, R., Che, T., Wang, W., Hu, X., Xu, Z., Wen, J., and Wang, L.: A multiscale dataset for

790   understanding complex eco-hydrological processes in a heterogeneous oasis system, Scientific Data, 4, 170083,

791   10.1038/sdata.2017.83, 2017.

792   Li, X., Liu, S., Yang, X., Ma, Y., He, X., Xu, Z., Xu, T., Song, L., Zhang, Y., Hu, X., Ju, Q., and Zhang, X.: Upscaling

793   Evapotranspiration from a Single-Site to Satellite Pixel Scale, 10.3390/rs13204072, 2021.

794   Li, X., Liu, S., Li, H., Ma, Y., Wang, J., Zhang, Y., Xu, Z., Xu, T., Song, L., Yang, X., Lu, Z., Wang, Z., and Guo, Z.:

795   Intercomparison of Six Upscaling Evapotranspiration Methods: From Site to the Satellite Pixel, Journal of Geophysical

796   Research: Atmospheres, 123, 6777-6803, https://doi.org/10.1029/2018JD028422, 2018.

797   Liu, H., Randerson, J. T., Lindfors, J., Massman, W. J., and Foken, T.: Consequences of Incomplete Surface Energy Balance

798   Closure for CO2 Fluxes from Open-Path CO2/H2O Infrared Gas Analysers, Boundary-Layer Meteorology, 120, 65-85,

799   10.1007/s10546-005-9047-z, 2006.

800   Liu, J., Chen, J. M., Cihlar, J., and Chen, W.: Net primary productivity distribution in the BOREAS region from a process

801   model using satellite and surface data, Journal of Geophysical Research: Atmospheres, 104, 27735-27754,

802   https://doi.org/10.1029/1999JD900768, 1999.

803   Liu, S., Xu, Z., Song, L., Zhao, Q., Ge, Y., Xu, T., Ma, Y., Zhu, Z., Jia, Z., and Zhang, F.: Upscaling evapotranspiration

804   measurements from multi-site to the satellite pixel scale over heterogeneous land surfaces, Agricultural and Forest

805   Meteorology, 230-231, 97-113, https://doi.org/10.1016/j.agrformet.2016.04.008, 2016.

806   Liu, S., Li, X., Xu, Z., Che, T., Xiao, Q., Ma, M., Liu, Q., Jin, R., Guo, J., Wang, L., Wang, W., Qi, Y., Li, H., Xu, T., Ran,

807   Y., Hu, X., Shi, S., Zhu, Z., Tan, J., Zhang, Y., and Ren, Z.: The Heihe Integrated Observatory Network: A Basin-Scale Land

808   Surface Processes Observatory in China, Vadose Zone Journal, 17, 180072, https://doi.org/10.2136/vzj2018.04.0072, 2018.

809   Mahrt, L.: Flux Sampling Errors for Aircraft and Towers, Journal of Atmospheric and Oceanic Technology, 15, 416-429,

810   https://doi.org/10.1175/1520-0426(1998)015<0416:FSEFAA>2.0.CO;2, 1998.

811   Massman, W. and Clement, R.: Uncertainty in Eddy Covariance Flux Estimates Resulting from Spectral Attenuation, in:

812   Handbook of Micrometeorology: A Guide for Surface Flux Measurement and Analysis, edited by: Lee, X., Massman, W., and

813   Law, B., Springer Netherlands, Dordrecht, 67-99, 10.1007/1-4020-2265-4_4, 2005.

814   Mathez, E. and Smerdon, J.: Climate Change3. Ocean– Atmosphere Interactions, in: The Science of Global Warming and Our

815   Energy Future, Columbia University Press, 69-100, doi:10.7312/math17282-005, 2018.

816   Mauder, M., Cuntz, M., Drüe, C., Graf, A., Rebmann, C., Schmid, H. P., Schmidt, M., and Steinbrecher, R.: A strategy for

817   quality and uncertainty assessment of long-term eddy-covariance measurements, Agricultural and Forest Meteorology, 169,

818   122-135, https://doi.org/10.1016/j.agrformet.2012.09.006, 2013.

819   Mayer, J., Mayer, M., Haimberger, L., and Liu, C.: Comparison of Surface Energy Fluxes from Global to Local Scale, Journal

820   of Climate, 35, 4551-4569, 10.1175/JCLI-D-21-0598.1, 2022.

821   Metzger, S., Junkermann, W., Butterbach-Bahl, K., Schmid, H. P., and Foken, T.: Measuring the 3-D wind vector with a

822   weight-shift microlight aircraft, Atmos. Meas. Tech., 4, 1421-1444, 10.5194/amt-4-1421-2011, 2011.

823   Metzger, S., Junkermann, W., Mauder, M., Beyrich, F., Butterbach-Bahl, K., Schmid, H. P., and Foken, T.: Eddy-covariance

824   flux measurements with a weight-shift microlight aircraft, Atmos. Meas. Tech., 5, 1699-1717, 10.5194/amt-5-1699-2012, 2012.

825   Mohan, M. M. P., Rajitha, K., and Murari, R. R. V.: Review of approaches for the estimation of sensible heat flux in remote

826   sensing-based evapotranspiration models, Journal of Applied Remote Sensing, 14, 1-31, 10.1117/1.JRS.14.041501, 2020.

827   Peltola, O., Aslan, T., Ibrom, A., Nemitz, E., Rannik, Ü., and Mammarella, I.: The high-frequency response correction of eddy

828   covariance fluxes – Part 1: An experimental approach and its interdependence with the time-lag estimation, Atmos. Meas.

829   Tech., 14, 5071-5088, 10.5194/amt-14-5071-2021, 2021.

830   Prudden, S., Fisher, A., Marino, M., Mohamed, A., Watkins, S., and Wild, G.: Measuring wind with Small Unmanned Aircraft

831   Systems, Journal of Wind Engineering and Industrial Aerodynamics, 176, 197-210,

832   https://doi.org/10.1016/j.jweia.2018.03.029, 2018.

833   Prueger, J. H., Hatfield, J. L., Parkin, T. B., Kustas, W. P., Hipps, L. E., Neale, C. M. U., MacPherson, J. I., Eichinger, W. E.,

834   and Cooper, D. I.: Tower and Aircraft Eddy Covariance Measurements of Water Vapor, Energy, and Carbon Dioxide Fluxes

835   during SMACEX, Journal of Hydrometeorology, 6, 954-960, 10.1175/JHM457.1, 2005.

836   Rannik, Ü., Peltola, O., and Mammarella, I.: Random uncertainties of flux measurements by the eddy covariance technique,

837   Atmos. Meas. Tech., 9, 5163-5181, 10.5194/amt-9-5163-2016, 2016.

838   Reineman, B. D., Lenain, L., Statom, N. M., and Melville, W. K.: Development and Testing of Instrumentation for UAV-

839   Based Flux Measurements within Terrestrial and Marine Atmospheric Boundary Layers, Journal of Atmospheric and Oceanic

840   Technology, 30, 1295-1319, 10.1175/JTECH-D-12-00176.1, 2013.

841 Reuder, J., Båserud, L., Jonassen, M. O., Kral, S. T., and Müller, M.: Exploring the potential of the RPA system SUMO for
842 multipurpose boundary-layer missions during the BLLAST campaign, Atmos. Meas. Tech., 9, 2675-2688, 10.5194/amt-9-
843 2675-2016, 2016.

844 Reuter, M., Bovensmann, H., Buchwitz, M., Borchardt, J., Krautwurst, S., Gerilowski, K., Lindauer, M., Kubistin, D., and
845 Burrows, J. P.: Development of a small unmanned aircraft system to derive CO_2 emissions of anthropogenic point sources,
846 Atmos. Meas. Tech., 14, 153-172, 10.5194/amt-14-153-2021, 2021.

847 Serrano-Ortiz, P., Kowalski, A. S., Domingo, F., Ruiz, B., and Alados-Arboledas, L.: Consequences of Uncertainties in CO_2
848 Density for Estimating Net Ecosystem CO_2 Exchange by Open-path Eddy Covariance, Boundary-Layer Meteorology, 126,
849 209-218, 10.1007/s10546-007-9234-1, 2008.

850 Sun, Y., Jia, L., Chen, Q., and Zheng, C.: Optimizing Window Length for Turbulent Heat Flux Calculations from Airborne
851 Eddy Covariance Measurements under Near Neutral to Unstable Atmospheric Stability Conditions, Remote Sensing, 10,
852 10.3390/rs10050670, 2018.

853 Sun, Y., Ma, J., Sude, B., Lin, X., Shang, H., Geng, B., Diao, Z., Du, J., and Quan, Z.: A UAV-Based Eddy Covariance System
854 for Measurement of Mass and Energy Exchange of the Ecosystem: Preliminary Results, Sensors, 21, 10.3390/s21020403,
855 2021a.

856 Sun, Y., Sude, B., Geng, B., Ma, J., Lin, X., Hao, Z., Jing, W., Chen, Q., and Quan, Z.: Observation of the winter regional
857 evaporative fraction using a UAV-based eddy covariance system over wetland area, Agricultural and Forest Meteorology, 310,
858 108619, https://doi.org/10.1016/j.agrformet.2021.108619, 2021b.

859 Tadić, J. M., Miller, S., Yadav, V., and Biraud, S. C.: Greenhouse gas fluxes from Alaska's North Slope inferred from the
860 Airborne Carbon Measurements campaign (ACME-V), Atmospheric Environment, 248, 118239,
861 https://doi.org/10.1016/j.atmosenv.2021.118239, 2021.

862 Thomas, R. M., Lehmann, K., Nguyen, H., Jackson, D. L., Wolfe, D., and Ramanathan, V.: Measurement of turbulent water
863 vapor fluxes using a lightweight unmanned aerial vehicle system, Atmos. Meas. Tech., 5, 243-257, 10.5194/amt-5-243-2012,
864 2012.

865 van den Kroonenberg, A., Martin, T., Buschmann, M., Bange, J., and Vörsmann, P.: Measuring the Wind Vector Using the
866 Autonomous Mini Aerial Vehicle M2AV, Journal of Atmospheric and Oceanic Technology, 25, 1969-1982,
867 10.1175/2008JTECHA1114.1, 2008.

868 Vellinga, O. S., Dobosy, R. J., Dumas, E. J., Gioli, B., Elbers, J. A., and Hutjes, R. W. A.: Calibration and Quality Assurance
869 of Flux Observations from a Small Research Aircraft*, Journal of Atmospheric and Oceanic Technology, 30, 161-181,
870 10.1175/JTECH-D-11-00138.1, 2013.

871 Wang, H., Jia, G., Zhang, A., and Miao, C.: Assessment of Spatial Representativeness of Eddy Covariance Flux Data from
872 Flux Tower to Regional Grid, Remote Sensing, 8, 742, 2016.

873 Webb, E. K., Pearman, G. I., and Leuning, R.: Correction of flux measurements for density effects due to heat and water
874 vapour transfer, Quarterly Journal of the Royal Meteorological Society, 106, 85-100, https://doi.org/10.1002/qj.49710644707,
875 1980.

876 Williams, A. and Marcotte, D.: Wind Measurements on a Maneuvering Twin-Engine Turboprop Aircraft Accounting for Flow
877 Distortion, Journal of Atmospheric and Oceanic Technology, 17, 795-810, 10.1175/1520-
878 0426(2000)017<0795:WMOAMT>2.0.CO;2, 2000.

879 Witte, B. M., Singler, R. F., and Bailey, S. C. C.: Development of an Unmanned Aerial Vehicle for the Measurement of
880 Turbulence in the Atmospheric Boundary Layer, Atmosphere, 8, 10.3390/atmos8100195, 2017.

881 Wolfe, G. M., Kawa, S. R., Hanisco, T. F., Hannun, R. A., Newman, P. A., Swanson, A., Bailey, S., Barrick, J., Thornhill, K.
882 L., Diskin, G., DiGangi, J., Nowak, J. B., Sorenson, C., Bland, G., Yungel, J. K., and Swenson, C. A.: The NASA Carbon
883 Airborne Flux Experiment (CARAFE): instrumentation and methodology, Atmos. Meas. Tech., 11, 1757-1776, 10.5194/amt-
884 11-1757-2018, 2018.

885 Xu, S., Xu, S., Zhou, Y., Yue, S., Zhang, X., Gu, R., Zhang, Y., Qiao, Y., and Liu, M.: Long-Term Changes in the Unique and
886 Largest Seagrass Meadows in the Bohai Sea (China) Using Satellite (1974–2019) and Sonar Data: Implication for Conservation
887 and Restoration, Remote Sensing, 13, 856, 10.3390/rs13050856, 2021.

888 Yang, X., Yong, B., Ren, L., Zhang, Y., and Long, D.: Multi-scale validation of GLEAM evapotranspiration products over
889 China via ChinaFLUX ET measurements, International Journal of Remote Sensing, 38, 5688-5709,
890 10.1080/01431161.2017.1346400, 2017.

891 Zappa, C. J., Brown, S. M., Laxague, N. J. M., Dhakal, T., Harris, R. A., Farber, A. M., and Subramaniam, A.: Using Ship-
892 Deployed High-Endurance Unmanned Aerial Vehicles for the Study of Ocean Surface and Atmospheric Boundary Layer
893 Processes, Frontiers in Marine Science, 6, 10.3389/fmars.2019.00777, 2020.

894 Zhang, G., Zhang, J., and Meng, P.: Estimation of kilometer-scale heat fluxes over a hilly area in Northern China using an
895 optical-microwave scintillometer, Agricultural Water Management, 244, 106582,
896 https://doi.org/10.1016/j.agwat.2020.106582, 2021.

897 Zheng, C., Liu, S., Song, L., Xu, Z., Guo, J., Ma, Y., Ju, Q., and Wang, J.: Comparison of sensible and latent heat fluxes from
898 optical-microwave scintillometers and eddy covariance systems with respect to surface energy balance closure, Agricultural
899 and Forest Meteorology, 331, 109345, https://doi.org/10.1016/j.agrformet.2023.109345, 2023.

900